DRAFT

Detonation and DDT in Partially Water-Filled Pipes.

N. P. Bitter and J. E. Shepherd

Graduate Aeronautical Laboratories
California Institute of Technology
Pasadena, CA 91125

Explosion Dynamics Laboratory Report FM2012.001

Updated May 25, 2012

Abstract

This report investigates the propagation of detonations and deflagration-to-detonation transition (DDT) in horizontal pipes that are partially filled with water and contain a detonable gas mixture (stoichiometric H_2-O_2) in a lenticular volume over the water layer. Detonations are found to produce oblique shock waves below the water that focus at the bottom of the pipe, generating peak reflection pressures that are 4-6 times the peak pressure of the incident wave. The amplified pressure spikes are of short duration and are confined to a small area, so the overall pressure loading is only slightly increased. Meanwhile, the water damps the motion of the pipe by adding mass and thermally insulating the lower half of the pipe. Consequently, peak strains decrease as the water depth increases, despite the amplified peak pressures.

Detonations and DDT are not significantly affected by the water layer, although pressures behind the detonation decay more rapidly as the water depth increases. DDT occurred within a distance of 30-60 cm for every water height, and no clear relationship between transition distance and water depth was found. At the largest water height that was tested (0.92 pipe diameters), the thickness of the gas layer was 4mm, which is still larger than the detonation cell size of 1.4 mm.

Contents

List of Figures

List of Tables

1 Introduction

This report investigates the various ways that detonations and deflagration-to-detonation transition (DDT) in horizontal pipes are affected by water layers. While this subject has applications in several industries, perhaps the most important application is nuclear waste treatment. One noteable example is the Hanford site in Washington state, where a nuclear waste treatment facility is being constructed to process the billions of gallons of radioactive material left over from previous nuclear weapons programs. Much of this material consists of a liquid or viscous slurry that evolves hydrogen and nitrous oxide as byproducts of chemical reactions driven by radioactive decay [Mahoney et al., 2000]. Since these gases are detonable in sufficient concentrations, it is important to understand the effect this slurry would have on detonations and DDT if they were to occur.

To investigate the effect of the radioactive slurry, it is reasonable as a first approximation to use water as a proxy for the radioactive material. This was done previously by Akbar and Shepherd [2010], who recorded high speed video of DDT in square channel partially filled with water. They also recorded strain measurements for DDT over a water layer in a cylindrical pipe. That prior investigation was significantly extended by Bitter and Shepherd [2012], who focused on the three-dimensional effects of DDT and detonations over water layers in cylindrical pipes. The present report is supplementary to that paper, serving to provide additional details about the experiments and analysis and a comprehensive listing of all the data that was taken related to the project.

2 Experimental Setup

The test specimen consists of two schedule 40, stainless steel tubes with inner diameter d = 52.5 mm, fitted with flanges on the ends. Dimensions and relevant material properties of the tubes are available in Table 1. These tubes are joined together with an aluminum plate partially blocking the junction between the two tubes, as shown in Fig. 1. Water can then be added to the left tube until the water depth reaches the blockage height h; the right tube meanwhile contains only the gas mixture.

Table 1: Material properties and dimensions of schedule 40, stainless steel pipe.

Property	**Units**	**Value**
Total length	m	2.32
Length of water-filled section	m	1.53
Length of gas-filled section	m	0.79
Outer diameter	mm	60.3
Inner diameter	mm	52.5
Wall thickness δ	mm	3.9
Total gas volume	L	5.2
Elastic Modulus E	GPa	193
Density ρ_s	kg/m^3	8040
Poisson's ratio ν	–	0.3
Thermal expansion coefficient	K^{-1}	16.9 x 10^{-6}

A schematic of the gas-supply system is shown in Fig. 2. The test section is initially evacuated to less than 100 mTorr, after which fuel and oxidizer are added by partial pressures and mixed for 5-10 minutes using a circulation pump. For shots with water, the fuel and oxidizer (stoichiometric H_2-O_2 at 300 K) are filled to a pressure less than the target ignition pressure of 1 bar. After mixing with the circulation pump, water is added until the target pressure of 1 bar is reached. Selected thermodynamic properties of the gas mixture are provided in Table 2.

2.1 Test Section Volumes

In order for this process to produce the desired water depth, the volume of the entire test section (including fill lines) and the target volume of the water to be added must be known. The test section volume was measured by attaching a vessel of known volume to the test section with an isolation valve between them. With the isolation valve closed, the test section was evacuated and the calibration volume pressurized to a known pressure. The isolation valve was then opened,

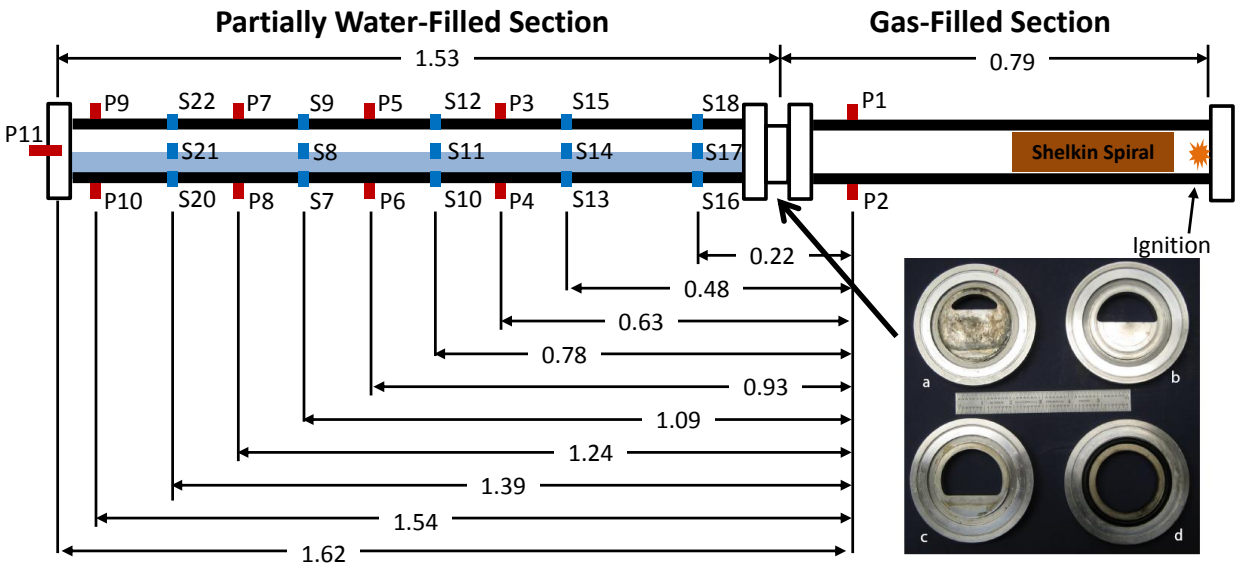

Figure 1: Diagram of experimental setup

Table 2: Thermodynamic properties of gas mixture.

Property	**Units**	**Value**
Pre-shot pressure	kPa	100
Pre-shot temperature	K	300
H_2 mole fraction	–	2/3
O_2 mole fraction	–	1/3
CJ Speed U_{CJ}	m/s	2834
CJ Pressure P_{CJ}	MPa	1.87
CJ Reflection Pressure	MPa	4.57
Detonation cell width [Kaneshige and Shepherd, 1997]	mm	1.39

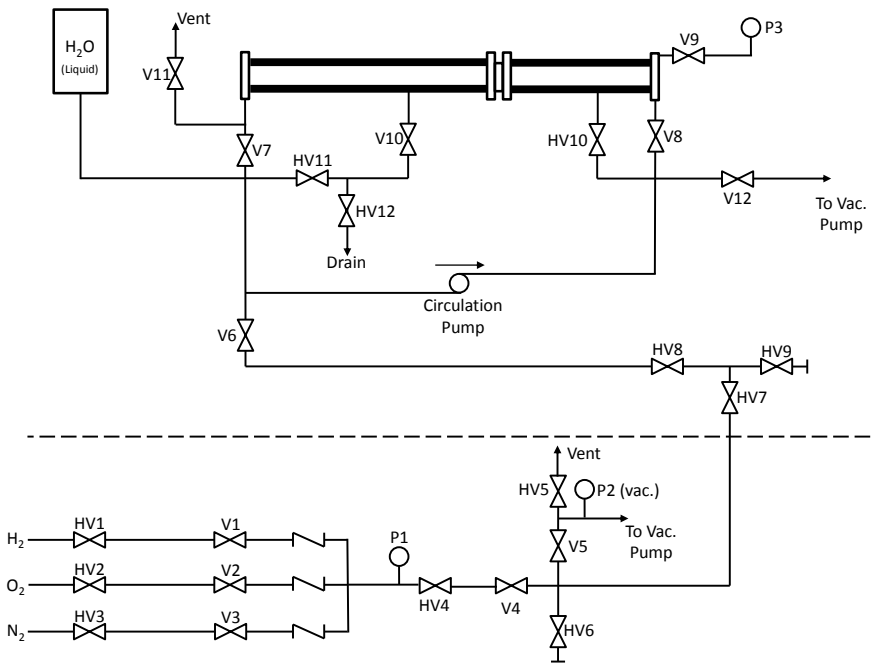

Figure 2: Schematic of gas supply system

allowing the pressure to equalize. After thermal equilibrium was reached, the final pressure was recorded and used to infer the test section volume. This process was also repeated in reverse by pressurizing the test section and evacuating the calibration volume. In both cases, the inferred test section volume was 5.19 L.

For a given water height, the volume of water required was also measured. This was done by filling left-hand side of the test section (see Fig. 1) until the water first began to overflow the blockage plate. The water was then drained and its volume measured. This was done for all water heights used in this experiment. The required gas fill pressure (before water addition) was then calculated using the following formula:

$$p_{initial} = p_{target}\left(\frac{V_{total} - V_{H2O}}{V_{total}}\right) \tag{1}$$

Post-shot measurements of water height and water volume confirmed that the desired water heights and volumes were reached.

2.2 Ignition and Data Acquisition

Two modes of ignition were used in this experiment. For detonations, a spark plug and Shchelkin spiral were installed at the water-free end of the tube, as depicted in Fig. 1. Transition to detonation then occurred before the detonation reached the water-filled portion of the tube. The detonation then passed through the blockage plate and over the surface of the water. For DDT, the Shchelkin spiral was removed and the spark plug was relocated to the port labeled P9 in Fig. 1. Transition to detonation then occurred over the surface of the water.

As shown in Fig. 1, pressure was measured at six increments along the tube axis. Pressure measurements were made using piezo-electric pressure transducers (PCB model 113B22), which have a rise time of less than 1 μs and a discharge time constant greater than 500 ms. At each location of pressure measurement, transducers were installed at both the top and bottom of the tube so that pressures could be measured above and below the water. Hoop strain was also measured at five locations along the tube axis. At each of these locations, strain gauges were attached at the top, side, and bottom of the tube. Strain measurements were made using gauges from Vishay PG, model CEA-09-250-UN. Strain gauge signals were amplified using a Vishay 2310B signal conditioner with a bandwidth of 155kHz. All pressure and strain measurements were simultaneously sampled at a rate of 1MHz.

3 Results

3.1 Detonations

Fig. 3 compares two pressure traces with no water (left) and a layer of water of thickness h/d = 0.50 (right). The addition of water has little effect on the pressure traces above the water, but at the bottom of the pipe the pressure traces are quite different; a series of regularly-spaced pressure spikes appears below the water.

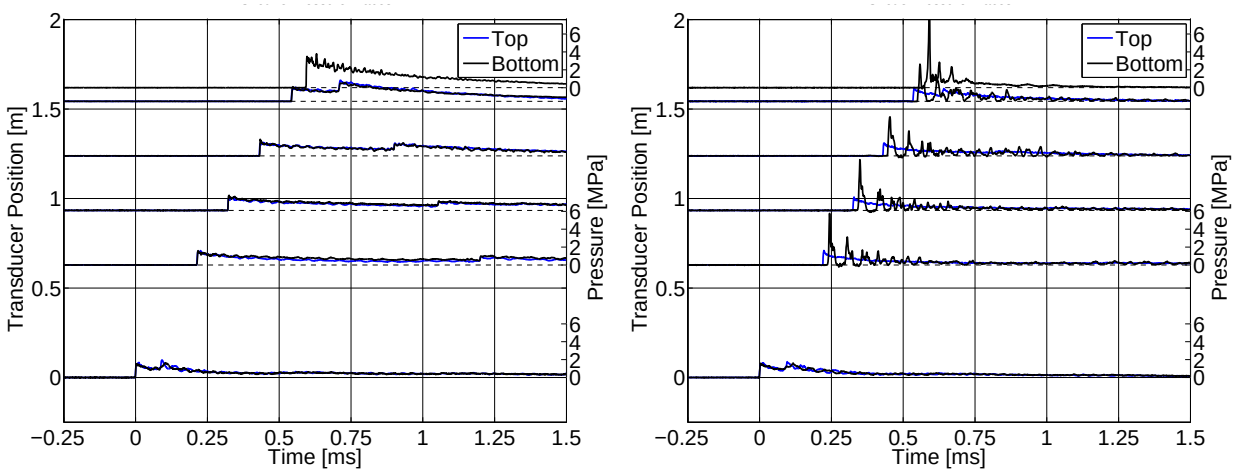

Figure 3: Typical pressure traces for a detonation with h/d = 0 (left) and h/d = 0.50 (right)

These pressure spikes are caused by an oblique shock wave system below the water, as depicted in Fig. 4. This schematic ignores the three dimensional effects that are present in the pipe, but portrays many of the important features of the interaction between the detonation and the water. Immediately behind the detonation, an oblique compressive wave travels down to the bottom of the pipe. Upon reaching the solid wall, the wave reflects back towards the free surface as a compression wave of greater magnitude. When the reflected wave reaches the free surface, it reflects again and becomes an expansion wave. This process produces a series of oblique waves behind the detonation, which alternate between tension and compression with each reflection from the free surface. Fig. 4 also portrays cavitation that may occur during due the expansion waves, as well as the surface deformation and breakup. These effects are discussed in more detail by Bitter and Shepherd [2012], who show that the surface remains undeformed for about 100 μs after the detonation passes.

Since the pressure jump across the detonation satisfies $\frac{\Delta p}{\rho c U} \sim 0.0004 << 1$, the linear acoustic approximation is satisfactory below the water, and hence the flow deflection angle is small and the

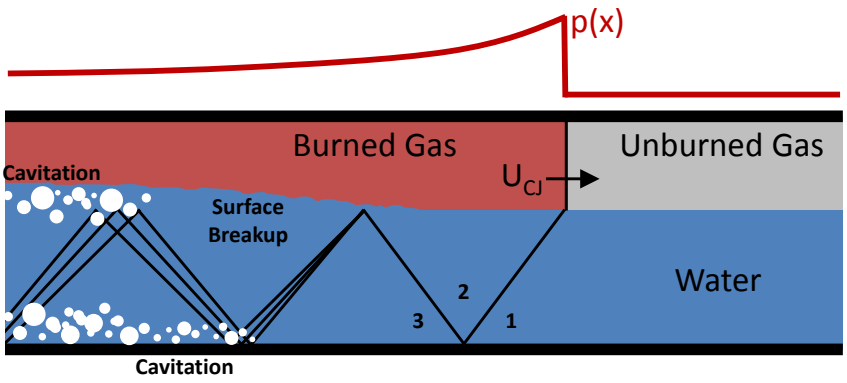

Figure 4: Two dimensional schematic of a detonation wave moving faster than the sound speed of water

p-θ diagram remains linear over the range of flow deflections that may occur. As a first approximation, one might model the flow in the round pipe as 2D channel flow. Under this assumption, the angle of the oblique waves below the water is easily computed from the detonation speed U and the acoustic speed c :

$$\alpha = \sin^{-1}\left(\frac{c}{U}\right) = \sin^{-1}\left(\frac{1484m/s}{2834m/s}\right) = 31.6^{\circ} \tag{2}$$

Furthermore, since the flow is acoustic, the angle of incidence equals the angle of reflection when the oblique waves reflect off of the bottom of the channel. The normal velocity jump across the oblique wave is equal to $\Delta w = \Delta p/\rho c$, and in order to satisfy the wall tangency condition the same Δw and Δp must occur across the reflected oblique wave. Hence the peak pressure expected in 2D channel flow is given by:

$$p_3 = p_1 + 2(p_2 - p_1) \sim 2p_2 \tag{3}$$

where the approximation is made for $p_2 >> p_1$. This 2D linear acoustic analysis predicts a peak reflection pressure of twice the peak detonation pressure, which is inconsistent with the experimental observations in Fig. 3, where peak pressures below the water are 3-4 times the incident pressure. As will be seen, this pressure amplification is caused by three-dimensional effects.

3.1.1 Modeling

Model Formulation To investigate the three dimensional wave motion below the water, a theoretical model was developed. It was established in Section 3.1 that the linearized acoustic equations are appropriate below the water, and that the free surface does not deform significantly until a long time (greater than one wave reflection) after the detonation passes. Based on these observations, the wave motion below the water was modeled using the linearized wave equation in cylindrical coordinates:

$$\frac{\partial^2 p}{\partial t^2} = c^2 \left(\frac{\partial^2 p}{\partial r^2} + \frac{1}{r}\frac{\partial p}{\partial r} + \frac{1}{r^2}\frac{\partial^2}{\partial \theta^2} + \frac{\partial^2 p}{\partial x^2} \right) \tag{4}$$

The pressure loading by the detonation wave, denoted $p_d(x,t)$, can be modeled quite accurately as a traveling wave which is a function only of the composite time variable $t' = x/U - t$, where x is the axial coordinate and U is the detonation velocity. Immediately behind the detonation wave, then, the solution is then expected to be of the form $p = p(x/U - t, r, \theta)$. This means that the problem can be greatly simplified by transforming into a frame of reference which is fixed to the detonation wave. After making this transformation, the 3D wave equation reduces to a 2D wave equation with a modified wave speed:

$$\frac{\partial^2 p}{\partial t^2} = \left(\frac{c^2}{1 - \frac{c^2}{U^2}} \right) \left(\frac{\partial^2 p}{\partial r^2} + \frac{1}{r}\frac{\partial p}{\partial r} + \frac{1}{r^2}\frac{\partial^2 p}{\partial \theta^2} \right) \tag{5}$$

Since the detonation speed in the experiments is greater that the sound speed of water, only the case $U > c$ is considered here. As mentioned earlier, surface motion is small for short times (less than about 100 μs) behind the detonation, so appropriate initial and boundary conditions are:

$$\begin{aligned} \left.\frac{\partial p}{\partial t'}\right|_{t'=0} &= 0 \\ \left.\frac{\partial p}{\partial r}\right|_{r=a} &= 0 \\ p(\theta = 0) = p(\theta = \pi) &= p_d(t') \end{aligned} \tag{6}$$

The detonation pressure $p_d(t')$ was modeled by fitting the experimental data with an exponentially decaying curve of the form:

$$p_d(t') = p_2 + (p_1 - p_2)\exp\left(-\frac{t'}{\tau_d}\right) \tag{7}$$

where p_1 is the peak detonation pressure, p_2 is the pressure towards which the pressure decays, and τ_d is the time constant governing the rate of pressure decay.

The system of Eqs. 5-6 is a homogeneous equation with non-homogeneous boundary conditions. To solve this system, it is convenient to make the cange of variables $\bar{p} = p - p_d(t')$ so that the boundary conditions become homogeneous. Making this change of variables, the wave equation becomes:

$$\frac{\partial^2 \bar{p}}{\partial t'^2} = \bar{c}^2 \left(\frac{\partial^2 \bar{p}}{\partial r^2} + \frac{1}{r}\frac{\partial \bar{p}}{\partial r} + \frac{1}{r^2}\frac{\partial^2 \bar{p}}{\partial \theta^2} \right) + \frac{\partial^2}{\partial t'^2} p_d(t') \tag{8}$$

where $\bar{c}^2 = c^2/(1 - c^2/U^2)$ is the effective wave speed introduced by the transformation to a wave-fixed coordinate system.

The method of separation of variables can be used to readily show that the homogeneous solution to the above equation is of the following form:

$$\bar{p}_h(r, \theta, t') = \sum_{m=1}^{\infty} \sum_{n=1}^{\infty} A_{mn} J_n(\lambda_m r) \sin(n\theta) \cos(\lambda_m c t') \tag{9}$$

where J_n is the nth order Bessel function of the first kind, and λ_m is the mth root of the equation $J_n(\lambda_m a) = 0$. These homogeneous eigenfunctions can now be used to solve the nonhomogeneous problem by assuming a solution of the following form:

$$\bar{p}(r, \theta, t') = \sum_{m=1}^{\infty} \sum_{n=1}^{\infty} P_{mn} J_n(\lambda_m r) \sin(n\theta) \tag{10}$$

$$p_d(t') = \sum_{m=1}^{\infty} \sum_{n=1}^{\infty} D_{mn} J_n(\lambda_m r) \sin(n\theta) \tag{11}$$

Upon substitution into Eq. 8, the following equation is obtained:

$$\ddot{P_{mn}} J_n(\lambda_m r) = \bar{c}^2 \left(J_n''(\lambda_m r) + \frac{1}{r} J_n'(\lambda_m r) - \frac{n^2}{r^2} J_n(\lambda_m r) \right) P_{mn} + \ddot{D_{mn}} J_n(\lambda_m r) \tag{12}$$

If the quantity $P_{mn}\lambda_m^2 \bar{c}^2 J_n(\lambda_m r)$ is added to both sides, then the terms in parenthesis are identically equal to zero, being a solution of Bessel's equation. The terms that remain are:

$$\ddot{P_{mn}} + P_{mn}\lambda_m^2 \bar{c}^2 = \ddot{D_{mn}} \tag{13}$$

This equation has the following homogeneous solution P_h:

$$P_h = A_{mn}\cos(\lambda_m \bar{c} t') + B_{mn}\sin(\lambda_m \bar{c} t') \tag{14}$$

The method of variation of parameters can be used to find particular solutions P_p of the form:

$$P_p = u_1(t')\cos(\lambda_m \bar{c} t') + u_2(t')\sin(\lambda_m \bar{c} t') \tag{15}$$

where u_1 and u_2 are functions to be determined. Using the usual techniques for the variation of parameters method (see, for example, Boyce and DiPrima [2009]), these functions are found to be:

$$u_1 = \frac{1}{\lambda_m \bar{c}} \int_0^{t'} \ddot{D}_{mn}\sin(\lambda_m \bar{c}\xi) d\xi \tag{16}$$

$$u_2 = \frac{-1}{\lambda_m \bar{c}} \int_0^{t'} \ddot{D}_{mn}\cos(\lambda_m \bar{c}\xi) d\xi \tag{17}$$

The general solution to Eq. 13 has now been found, and is of the following form:

$$P_{mn} = A_{mn}\cos(\lambda_m \bar{c} t') + B_{mn}\sin(\lambda_m \bar{c} t') + P_p(t') \tag{18}$$

where the particular solution P_p is defined by Eqs. 15, 16, and 17. When the initial conditions $\dot{P}(0) = 0$ and $P(0) = P_i(r, \theta, 0)$ are applied, the coefficient B_{mn} is found to be equal to zero. It remains to find the coefficients A_{mn} and D_{mn} by integrating the initial pressure distribution and the non-homogeneous term against the eigenfunctions and their respective weight functions. The results are:

$$A_{mn} = \frac{\int_0^R \int_0^\pi P(r,\theta,0) J_n(\lambda_m r)\sin(n\theta) r dr d\theta}{\int_0^R \int_0^\pi J_n(\lambda_m r)^2 \sin^2(n\theta) r dr d\theta} \tag{19}$$

$$D_{mn} = p_d(t') \frac{\int_0^R \int_0^\pi J_n(\lambda_m r)\sin(n\theta) r dr d\theta}{\int_0^R \int_0^\pi J_n(\lambda_m r)^2 \sin^2(n\theta) r dr d\theta} \tag{20}$$

In summary, the complete solution is expressed as follows:

$$p(r,\theta,t') = \bar{p}(r,\theta,t') + p_d(t') \tag{21}$$

$$= p_d(t') + \sum_{m=0}^{\infty}\sum_{n=0}^{\infty} P_{mn}(t') J_n(\lambda_m r)\cos(n\theta) \tag{22}$$

where

$$P_{mn}(t') = A_{mn}\cos(\lambda_m \bar{c} t') + P_p(t') \tag{23}$$

$$P_p(t') = \frac{\cos(\lambda_m \bar{c} t')}{\lambda_m \bar{c}} \int_0^{t'} \ddot{D}_{mn} \sin(\lambda_m \bar{c}\xi) d\xi + \frac{\sin(\lambda_m \bar{c} t')}{\lambda_m \bar{c}} \int_0^{t'} \ddot{D}_{mn} \cos(\lambda_m \bar{c}\xi) d\xi \tag{24}$$

$$A_{mn} = \frac{\int_0^R \int_0^\pi P(r,\theta,0) J_n(\lambda_m r)\sin(n\theta) r dr d\theta}{\int_0^R \int_0^\pi J_n(\lambda_m r)^2 \sin^2(n\theta) r dr d\theta} \tag{25}$$

$$\ddot{D}_{mn} = \frac{\partial^2 p_d}{\partial t'^2} \frac{\int_0^R \int_0^\pi J_n(\lambda_m r)\sin(n\theta) r dr d\theta}{\int_0^R \int_0^\pi J_n(\lambda_m r)^2 \sin^2(n\theta) r dr d\theta} \tag{26}$$

3.1.2 Model Results

Before making predictions with this model, it is necessary to ensure that it is sufficiently resolved. A convergence study was conducted with 50, 100, and 200 terms in each of the double series in Equation 22. Pressure traces at θ = 90° (the bottom of the pipe) and 45° are overlaid in Fig. 5 and are compared also with experimental pressure traces. This plot shows reasonable qualitative convergence of the model as the resolution is increased. Although 50 or 100 terms seems to provide sufficiently converged results, all future model predictions presented in this report are made with 200 terms. It should be noted that Fourier series approximations to functions with sharp discontinuities can produce spurious peaks near the discontinuity which do not disappear with an increased number of terms (the Gibbs phenomenon). For example, if a square wave is approximated by a Fourier series, overshoot near the discontinuity approaches a constant value of about 9% as the number of terms approaches infinity. Although the series solution approach may predict pressures that are slightly high near the shock waves, this method has the advantage that it produces no artificial dispersion of wavefronts; in fact, the accuracy with which the solution reproduces the initial conditions at t = 0 is the same as the accuracy at which the solution is modeled at any other time. Thus despite the slight innacuracies in the the predictions of pressure magnitude, this solution technique models the wave trajectories quite well.

The experimental pressure traces shown in Fig. 5 exhibit the same large scale behavior as the model predictions, but due to the limited temporal (and spatial) resolution of the transducers, the finer scale behavior is not captured. The diameter of the pressure transducer is about 5.5 mm, so a detonation traveling 2800 m/s will take about 2 μs to cross the transducer. The transducer's rise time is about 1 μs, so the transducer subjected to a perfectly sharp detonation wave at 2800 m/s would be expected to blur the sharp edge over a 2-3 μs interval. This corresponds well with the measurements shown in Fig. 5. The comparison between experiment and theory shown here

gives some indication that the model is accurate, but not conclusive confirmation. In Section 3.1.3, additional experimental data will be used to further validate this model.

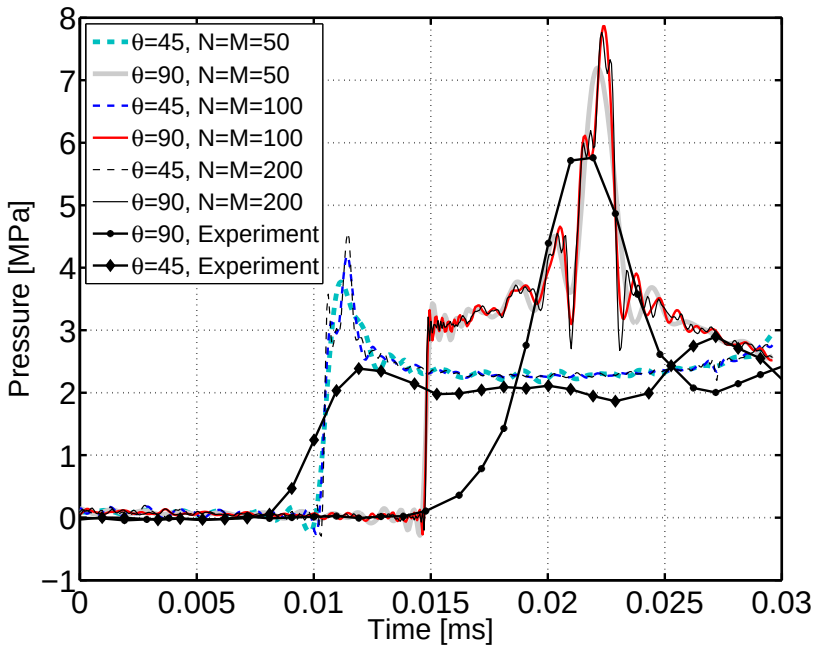

Figure 5: Comparison between experimental and theoretical pressure traces for various model resolutions.

A sequence of pressure contours as predicted by the model is shown in Fig. 6. The interaction between the incident shock wave and the wall produces a pair of reflected shocks that sweep along the pipe walls and merge at the base of the pipe, producing the short-duration, high-pressure spike observed in experiments. The interaction between the planar incident shock wave and the wall can be much more complicated, especially for stronger incident shocks. In general, the type of shock reflection that occurs depends on the shock strength, the pipe's radius of curvature, and the wall angle at which the incident wave initially meets the surface (meaning different behavior may result for different water depths). A more detailed discussion of the types of shock reflections that can occur is given by Ben-Dor [2007]. An interesting related study was conducted by Skews and Kleine [2007], who experimentally investigated the analogous problem of a weak (M=1.04) planar shock reflecting off of a concave cylindrical surface using schlieren photography, and produced schlieren images which are remarkably similar to the pressure contours in 6.

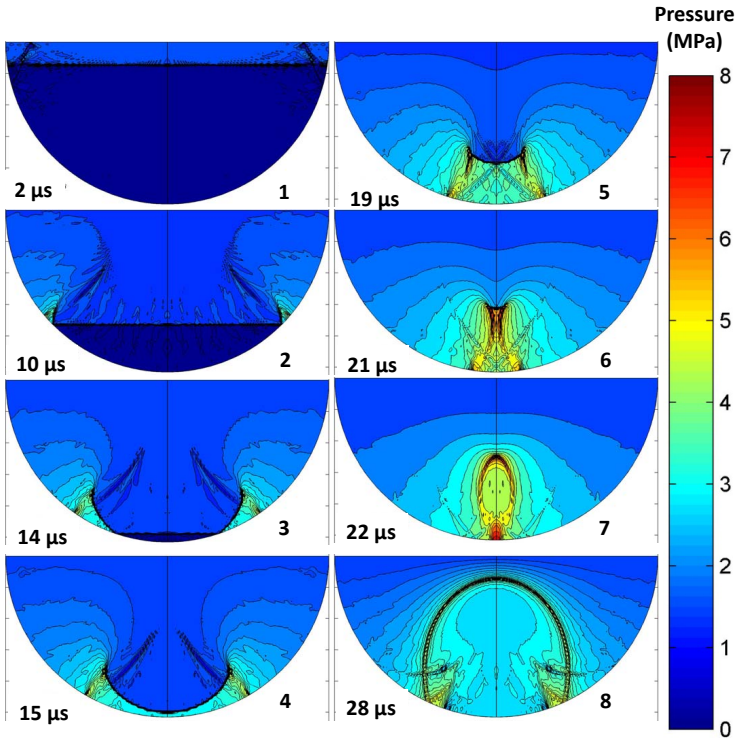

Figure 6: Sequence of pressure contours predicted by 2D model

3.1.3 Pressure vs. Angle

To provide further validation of the theoretical model, the variation of pressure with angular position was measured experimentally. The pipe was filled to a constant water depth of h/d = 0.50, and was rotated from 0° to 75° in 15° increments, so that pressure could be measured at various angular positions. Pressure and strain measurements in this setup are typically quite repeatable for detonations that are initiated using a Shchelkin spiral, which enables the pressure field to be pieced together using data from multiple shots. Experimental pressure contours plotted against time and angular position θ are shown in Fig. 7 and are compared with the predictions of the theoretical model in Fig. 8.

For the experimental pressure contours, two shots were recorded at each angle of pipe rotation. The data from one of these shots was plotted as positive θ and the other as negative θ. As a result, the symmetry of the contour plot about θ = 0 (the bottom of the pipe) is indicative of the repeatability of the data. For the modeled pressure contours, the predictions are only valid for the first 30 μs. After this point, the reflected wave reaches the free surface (see Fig. 6), and the model predicts negative pressures which would produce cavitation in experiments. During the period over which the model is valid, excellent agreement is seen with the experimental data.

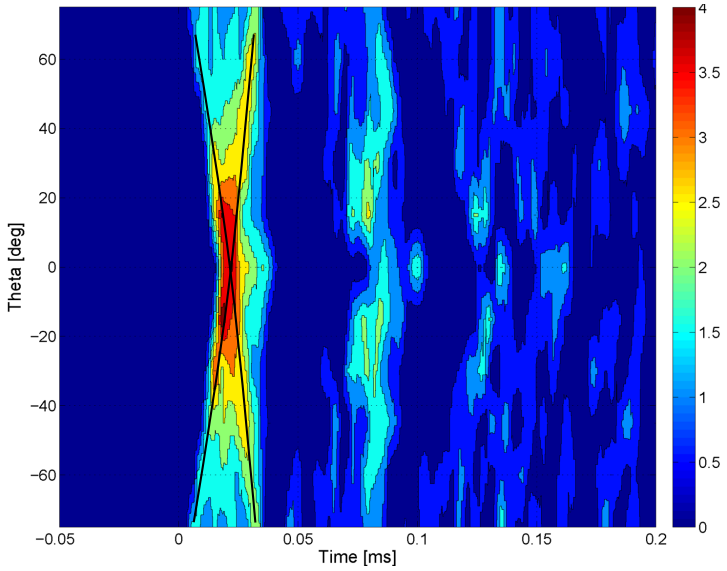

Figure 7: Contours of pressure P6 against time and θ for a detonation with $h/d = 0.50$. Pressures are normalized by the peak pressure of the detonation as measured above the water. The bottom of the pipe is denoted $\theta = 0$. Two shots were conducted for each angle; one is plotted as $+\theta$ and the other as $-\theta$.

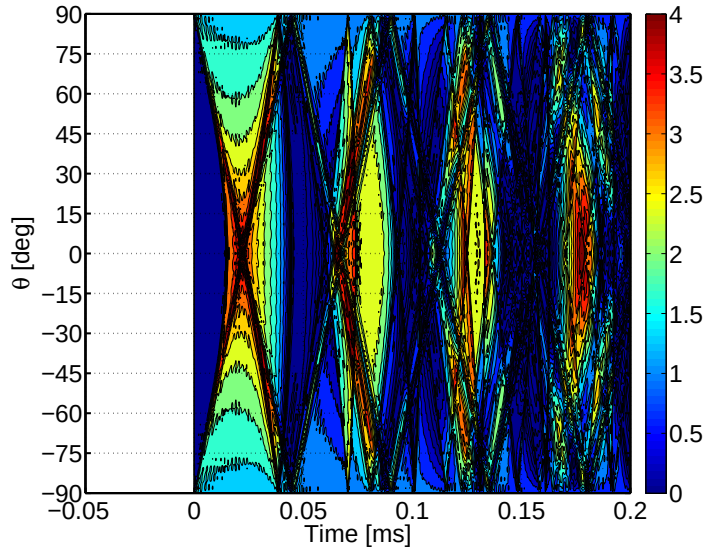

Figure 8: Theoretical contours of pressure) against time and θ. Pressures are normalized by the peak pressure above the water. Solution is only valid until $t = 30\ \mu s$.

After the reflected wave strikes the free surface (t >30 μs), the behavior of the shock system in the experimental data becomes very complicated. In addition to the geometrical complications, cavitation occurs and surface breakup and deformation start to become significant; these processes interfere with the wave's reflection from the free surface, resulting in scattering and dispersion of the wave. As a result, the second pressure wave is much less distinct, and subsequent waves are nearly indistinguishable.

3.1.4 Other water depths

Pressure traces for several other water heights are shown in Figs. 9 and 10. The period of the pressure spikes appears to increase in proportion with water depth. This is consistent with the supposition that the pressure spikes are caused by oblique waves below the surface, the wavelength of which are proportional to the water depth. At the highest water depths, it becomes clear that the high pressure spike due to shock focusing occurs only for a short time, on the order of a few microseconds. After this high pressure transient is over, the pressure at the bottom of the pipe plateaus to a relatively constant pressure of about twice the incident detonation pressure.

The detonation did not fail for any water depth, even for the deepest water depth of $h/d = 0.92$. This water depth corresponds to a gas layer thickness of about 4 mm, which is still larger than the detonation cell width of 1.4 mm. Gas layer thicknesses smaller than the detonation cell width were not tested in these experiments.

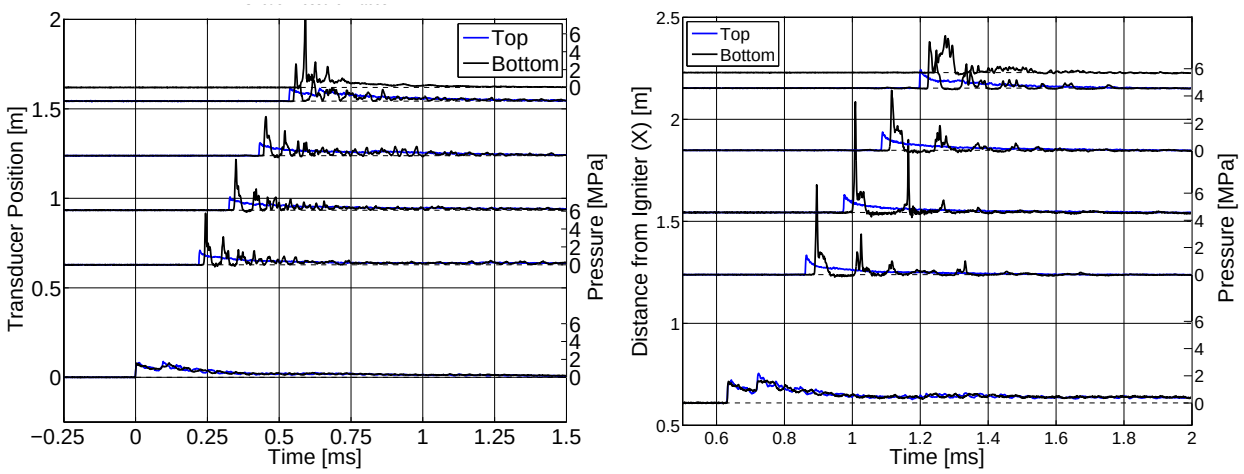

Figure 9: Typical pressure traces for a detonation with $h/d = 0.5$ (left) and $h/d = 0.75$ (right)

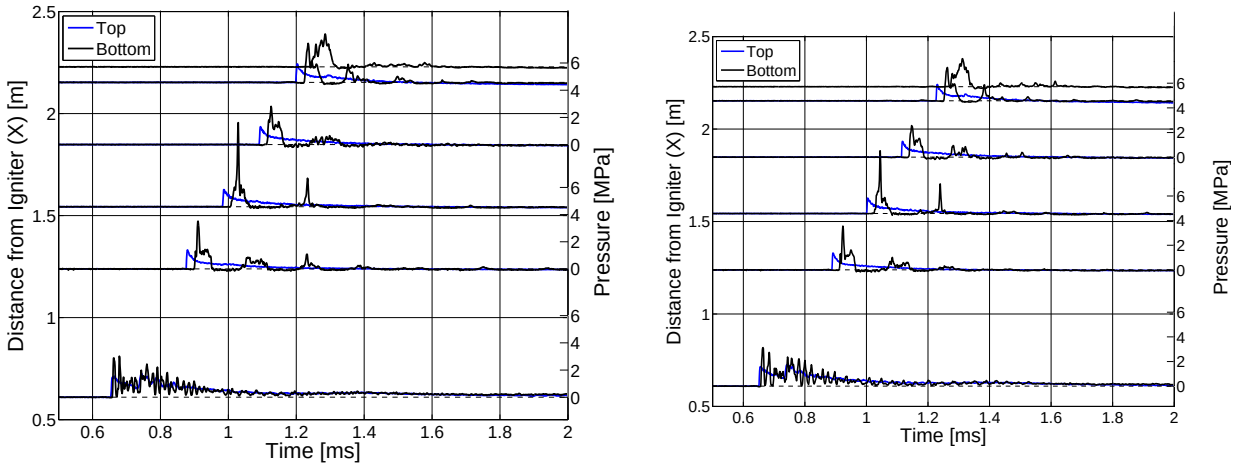

Figure 10: Typical pressure traces for a detonation with $h/d = 0.87$ (left) and $h/d = 0.92$ (right)

3.2 Transition to Detonation

In this section, transition to detonation over the surface of the water is studied. The experiment was modified by removing the Shchelkin spiral and relocating the spark plug to port P9 (see Fig. 1). Pressure traces for the various water heights are shown in Figs. 11-13. Transition to detonatioan occurred for every water height. However, at the highest water height of $h/d = 0.92$, the detonation failed as it passed from the water-filled section to the gas-filled section (this transition occurs at X=1.53 m). This behavior is consistent with experimental measurements of detonation diffraction taken by Benedick et al. [1985].

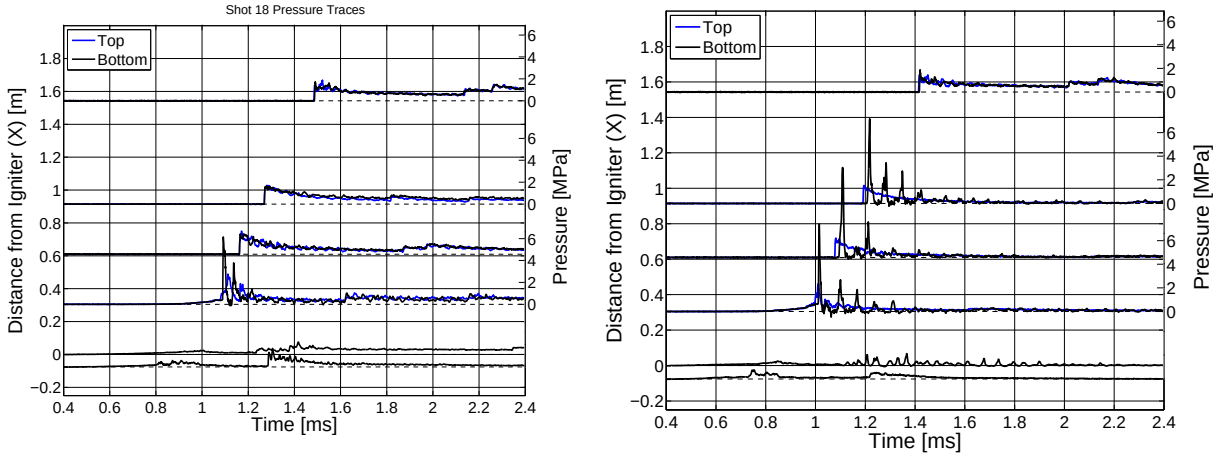

Figure 11: Typical pressure traces for a DDT with $h/d = 0$ (left) and $h/d = 0.5$ (right)

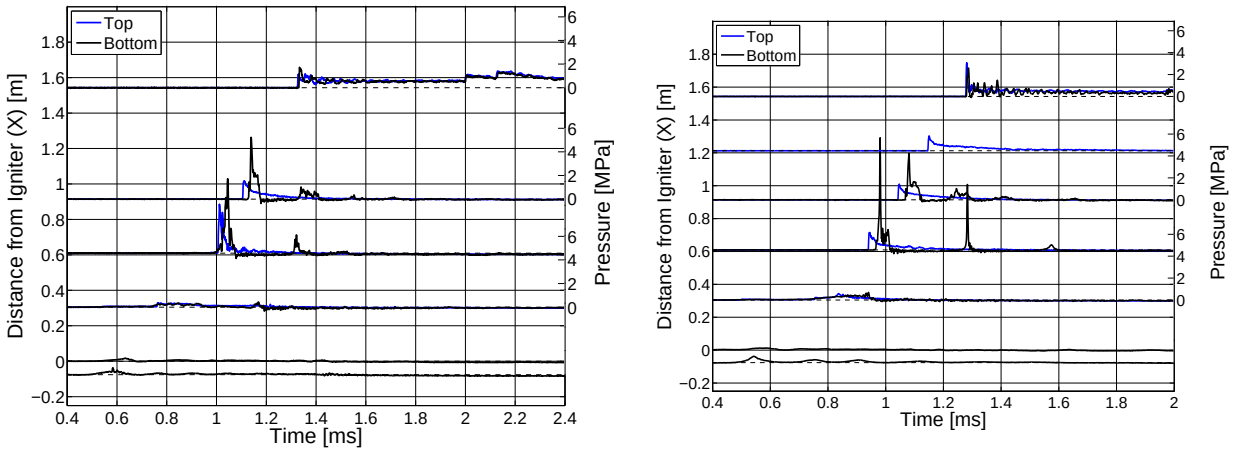

Figure 12: Typical pressure traces for a DDT with $h/d = 0.75$ (left) and $h/d = 0.87$ (right)

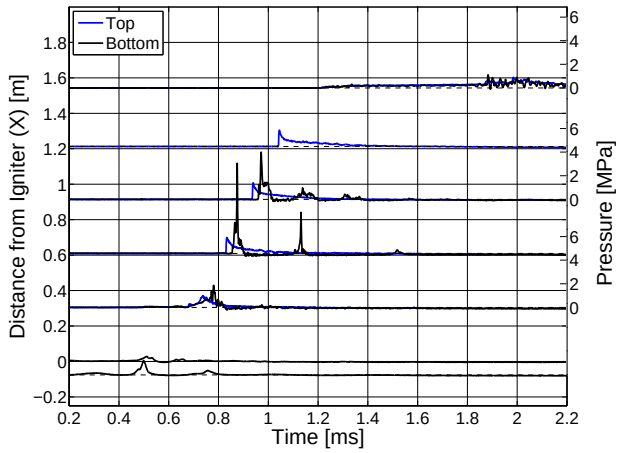

Figure 13: Typical pressure traces for a DDT with $h/d = 0.92$

3.2.1 Transition Distance

It has been shown that transition to detonation occurred at every water height. It is interesting to examine also whether or not the transition distance was affected by the water depth. The simplest way to determine the transition distance is to find the first pressure transucer at which the pressure trace above the water has the characteristic form of a detonation wave: no precursor and a sharp jump to approximately the CJ pressure. Unfortunately, since the pressure transducers are installed 30 cm apart, the transition distance measured using this method has an uncertainty of $\pm$ 15 cm, which is 20-50% of the transition distances themselves, which are about 30-80 cm. Since strain gauges are located between the pressure transducers, it is sometimes possible to use the strain traces to determine whether transition has occurred at a particular strain gauge location, thus reducing the uncertainty in transition distance to about $\pm$ 7 cm. However, it is not always possible to determine from a strain trace whether or not DDT has occurred, particularly in the water-filled cases.

To obtain more precise estimates of the transition distance, pressure and strain traces were plotted on an X-t diagram and lines were fit to the detonation wave and the "retonation" wave which propagates back towards the ignition point. The intersection between these two lines is a reasonable estimate of the location at which DDT occurred. An example of this process is shown in Fig. 14.

The same type of estimate can also be made using the strain traces. An alternative estimate is to find the intersection between the trajectory of the detonation and the precursor shock wave before the DDT event; this estimate also can be made using either pressure or strain data. Thus four different estimates of the transition distance are available which make use of either pressure or strain data and either the precursor shock or the retonation wave. Depending on the water depth

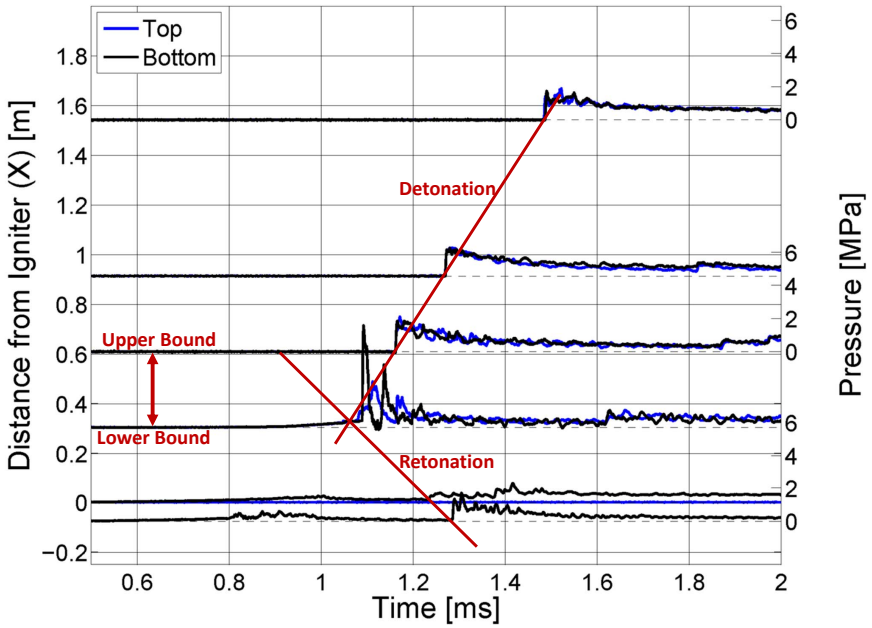

Figure 14: Estimate of transition distance using wave trajectories on an X-t diagram

and the actual DDT location, each of the four estimates may be very good or very poor, or not even useable. The transition distances estimated using these methods are summarized in Table 3, where each estimate has been assigned a qualitative rating of the confidence in the prediction.

Table 3: Transition Distances

Shot #	h/d	Transition Distance [m]										
		Based on Pressure Precursor Wave		Based on Pressure Retonation Wave		Based on Strain Precursor Wave		Based on Strain Retonation Wave		Lower Bound	Upper Bound	Best Estimate
18	0.00	NA	-	0.32	Excellent	0.35	Good	NA	-	0.30	0.45	0.32
71	0.00	NA	-	0.62	Excellent	0.70	Fair	0.62	Good	0.60	0.76	0.62
66	0.00	NA	-	0.62	Fair	0.62	Good	0.62	Excellent	0.60	0.76	0.62
67	0.00	NA	-	0.60	Fair	0.68	Fair	0.62	Excellent	0.60	0.76	0.62
72	0.00	NA	-	0.60	Fair	0.75	Poor	0.62	Excellent	0.60	0.76	0.62
69	0.25	NA	-	0.66	Good	0.66	Good	0.66	Good	0.60	0.76	0.66
70	0.25	NA	-	0.55	Poor	0.62	Good	0.62	Good	0.60	0.76	0.62
19	0.50	0.42	Poor	0.50	Fair	0.45	Good	NA	-	0.30	0.60	0.45
20	0.50	NA	-	0.60	Fair	0.50	Fair	0.66	Excellent	0.60	0.76	0.66
41	0.75	0.67	Very Poor	NA	NA	0.61	Poor	0.61	Fair	0.45	0.76	0.61
42	0.75	0.64	Very Poor	NA	NA	0.45	Poor	0.58	Fair	0.45	0.76	0.58
58	0.87	0.60	Very Poor	NA	NA	0.50	Very Poor	NA	-	0.30	0.61	0.60
64	0.92	0.52	Fair	NA	NA	0.50	Very Poor	NA	-	0.30	0.61	0.53
65	0.92	0.55	Fair	NA	NA	NA	-	NA	-	0.30	0.61	0.54

The data from Table 3 are plotted in Fig. 15. No clear trend is observed, though perhaps argument might be made that the transition distance decreases slightly at high water depths. The scatter in the data occurs because DDT can be strongly affected by small perturbations in the initial conditions, which can be interpreted as a stochastic aspect of the transition process. It appears that

to more completely understand the relationship between transition distance and water depth, it would be necessary to conduct a large number of shots and analyze that mean and spread of the transition distances as functions of water height.

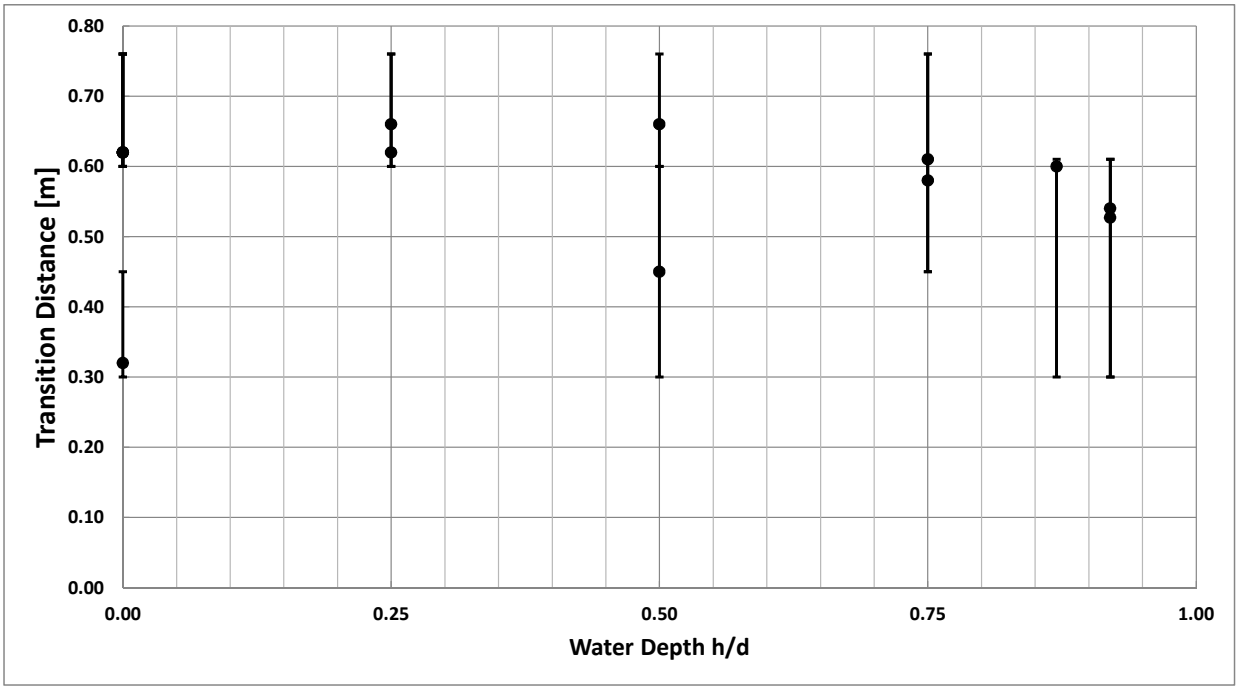

Figure 15: Relationship between transition distance and water height

In the results shown above, DDT occurred at every water height. The minimum ratio of gas layer thickness to detonation cell size was about 2.9. It is interesting to compare this result with data from a prior study by Akbar and Shepherd [2010]. These prior experiments were conducted using 30/70 H_2-N_2O at 1 atm and 300 K, rather than stoichiometric H_2-O_2 which is used in the present experiments. The H_2-N_2O mixture has a cell size of about 3-5 mm [Kaneshige and Shepherd, 1997], and the H_2-N_2O experiments were conducted with h/d = 0.81 and 0.88, which correspond to gas layer thicknesses of 6-10 mm. Thus the ratio of gas layer thickness to cell size was about 1.5-2.5. The resulting pressure traces are shown in Fig. 16. For the thicker gas layer (h/d = 0.81), transition occurred only at the very end of the test section, while for the thinner gas layer (h/d = 0.88), it did not occur at all. This seems to indicate that less sensitive mixtures may not be able to transition to detonation in the thin gas layer over the water, especially as the gas layer thickness approaches the cell size.

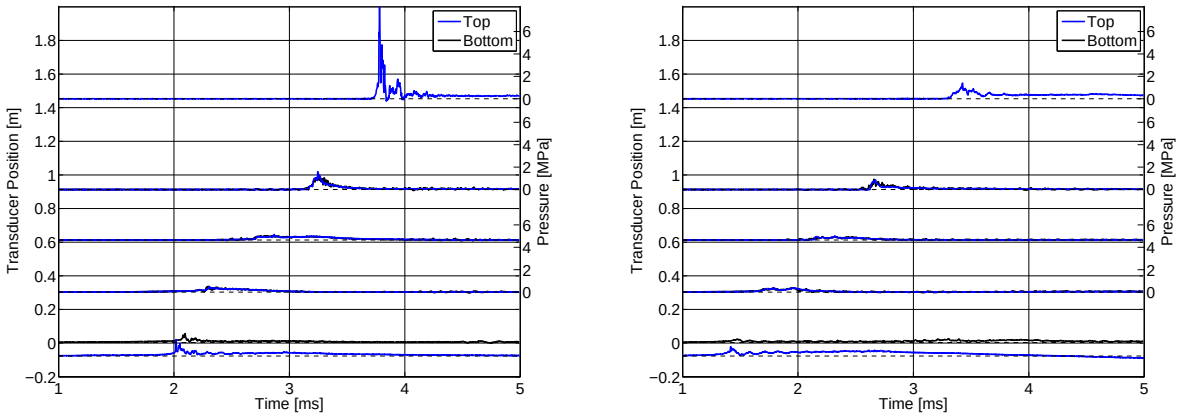

Figure 16: Pressure traces for DDT in H_2-N_2O with $h/d = 0.81$ (left) and $h/d = 0.88$ (right). Data is taken from Akbar and Shepherd [2010]. Ignition is at a transducer position of 0 m.

3.3 Structural Response

3.3.1 Vibrational Response

Having discussed the fluid dynamics of the interaction between the detonation and the water layer, we turn now to the structural loading of the tube. Typical strain traces for a detonation with no water are plotted in Fig. 17.

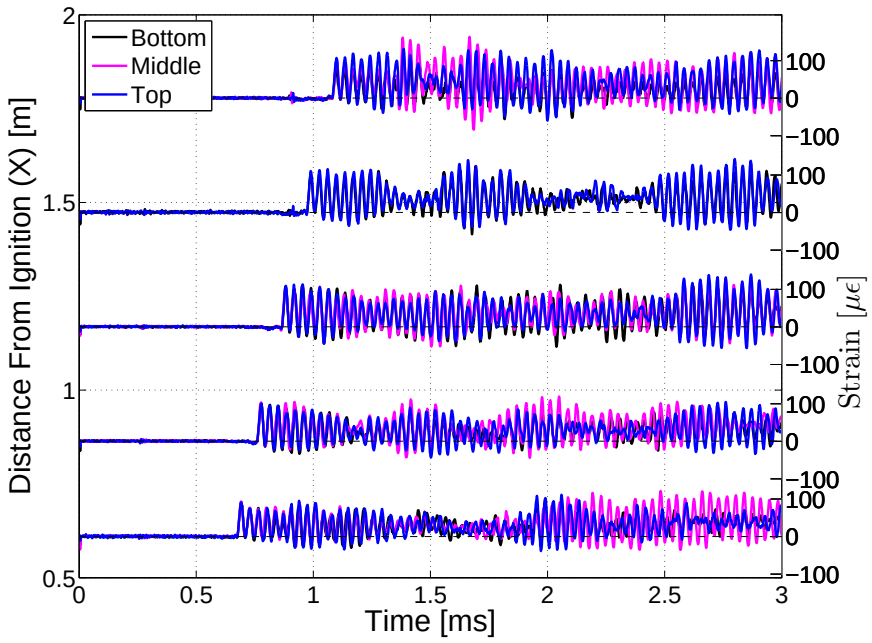

Figure 17: Hoop strain traces for a detonation with no water in pipe.

The signals from the three gauges at the top, side, and bottom of the tube oscillate in phase at 29 kHz, which is the natural frequency of the first, axisymmetric breathing mode given by Blevins [1979]:

$$\omega_n = \frac{1}{2\pi a}\sqrt{\frac{E}{\rho_s(1-\nu^2)}} \tag{27}$$

Strain traces for a detonation with water of depth h/d = 0.50 are shown in Fig. 18. The peak strain is reduced considerably, and the strain gauges at the top, side, and bottom of the tube no longer oscillate in phase. The added mass of the water likely contributes to this effect, but experiments have shown that heat transfer also plays a major role. The water layer insulates the bottom of the tube, resulting in a non-axisymmetric temperature distribution (this temperature distribution is analyzed in more detail in Section 3.4). This produces bending stresses which slightly distort the shape of the pipe and transfer energy from the axisymmetric hoop mode to

other non-axisymmetric modes. The result is that the energy of vibration is no longer concentrated at a single frequency, and hence the peak strains are reduced.

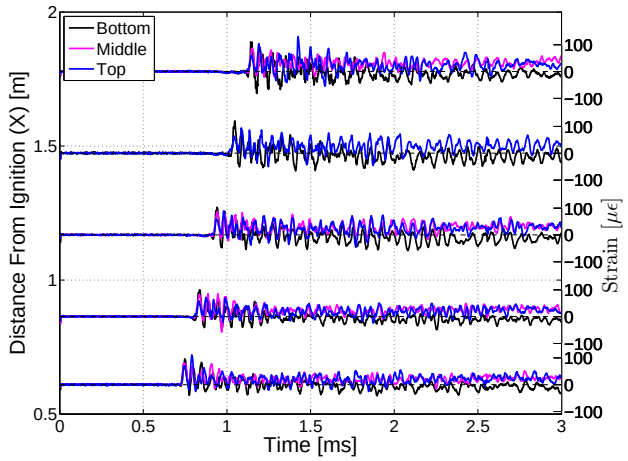

Figure 18: Hoop strain traces for a detonation with water depth h/d = 0.50.

This hypothesis was investigated experimentally by insulating a portion of the pipe with a thin neoprene sheet. This sheet covered only the bottom half of the pipe and, being only about 60 cm long, insulated only strain gauges S13-S18 (see Fig 1). Since the mass of the neoprene sheet is much less than that of the tube, it affects the vibrational response of the tube only by impeding heat transfer. Strain traces for the insulated tube are plotted in Fig. 19, where only the bottom two sets of gauges at x = 0.61 and 0.86 m are insulated. Clearly, the thin insulating sheet has a large impact on the vibrational response of the tube.

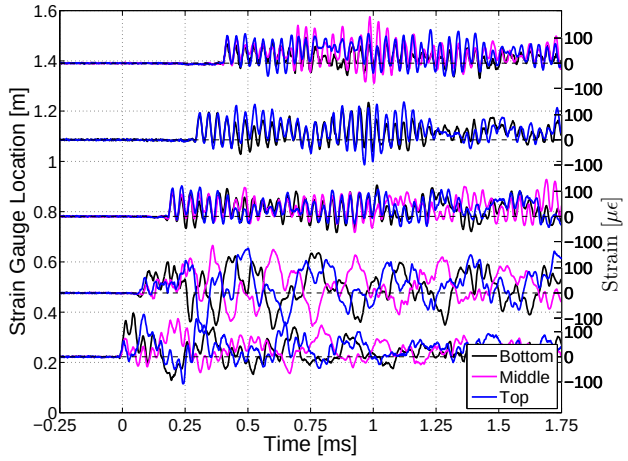

Figure 19: Strain traces for a detonation with a neporene sheet covering the bottom half of the pipe at the first two strain measurement locations (x = 0.61 and 0.86 m)

The vibrational response is more easily interpreted when characterized in frequency space. Fig. 20 shows ordinary and pre-multiplied power spectra of a strain traces for no water, $h/d = 0.50$, and neoprene insulation. The ordinary power spectrum shows the lower frequency peaks more clearly, while the pre-multiplied spectrum explicitly portrays the energy content of the peaks, which is proportional to the area under the curve.

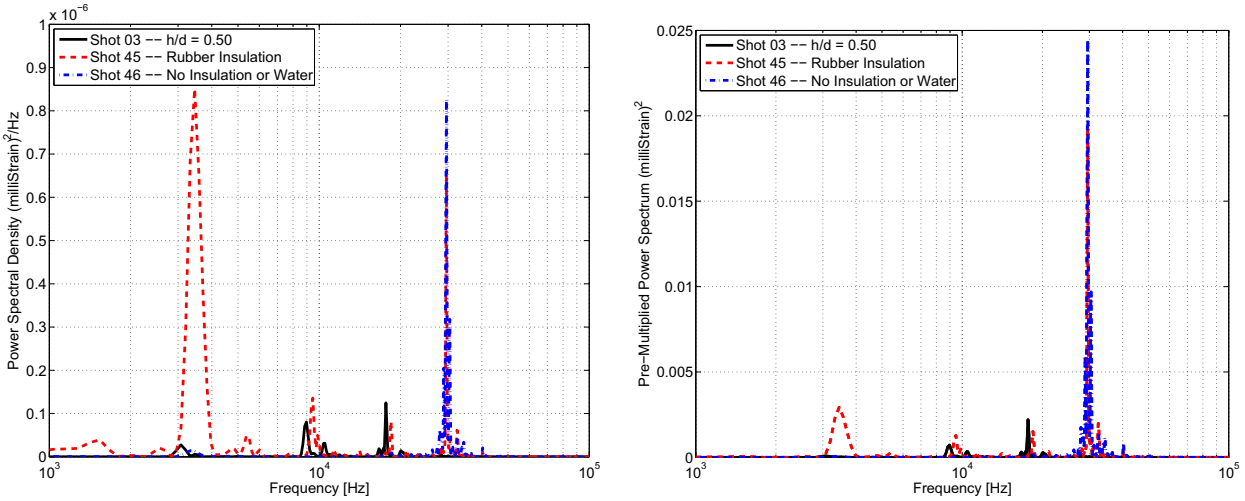

Figure 20: Ordinary (left) and pre-multiplied (right) power spectra for insulated, un-insulated, and water-filled tubes.

For the pipe with no water or insulation, the vibrational energy is concentrated almost entirely in the axisymmetric hoop mode, which has a natural frequency of 29 kHz (see Eq. 27). For both the water layer and neoprene insulation, the power spectra exhibit significant peaks at frequencies of 3.4, 9.4, and 17.6 kHz. These correspond very closely to the natural frequencies of the first three non-axisymmetric modes which Blevins [1979] terms the "radial-circumferential flexural modes." The first three of these modes have natural frequencies of 3.2, 8.9, and 17.1 kHz, which are very close to the experimental values reported above.

In the case of neoprene insulation, much of the vibrational energy is concentrated in the 2$^{\text{nd}}$ radial-circumferential mode which. Although the corresponding peak on the pre-multiplied power spectrum is not as large as the peak at 29 kHz, it is much broader and the area underneath (and hence energy contained) is about the same, if not slightly greater. In the water-filled case, comparatively little energy is concentrated in the 2$^{\text{nd}}$ mode; in fact, less energy is contained in the 2$^{\text{nd}}$ mode than in the 3$^{\text{rd}}$ and 4$^{\text{th}}$. It appears that for the water-filled case, a greater fraction of the total energy is retained in the axisymmetric mode and less is transferred to the higher order modes. This is consistent with the behavior shown in Figs. 18 and 19, where the 29 kHz oscillations are retained

more strongly in the water-filled case than in the rubber insulated case.

3.3.2 Peak Strains

In the preceding section, the water layer was shown to modify the vibrational response of the tube both by adding mass and by thermally insulating a portion of the tube wall. To investiage how greatly the water layer affects the peak strains, it is useful to normalized the strain measurements by defining a dynamic loading factor Φ:

$$\Phi = \frac{\epsilon_{max} E \delta}{P_{CJ} a} \tag{28}$$

where P_{CJ} is the CJ pressure, δ is the wall thickness, and ϵ_{max} is the peak strain. The dynamic amplification factor is plotted against water height for both detonations and DDT in Fig. 21, where in the case of detonations the peak strains are recorded prior to detonation reflection. For detonations with no water in the tube, the amplification factor is about 2.5; this is slightly greater than the value of 2 that is predicted for load speeds that significantly exceed the first critical velocity (see, for example, Beltman and Shepherd [2002]). In this case, the load speed of 2830 m/s is far above the first critical velocity of about 1450 m/s. The peak strain then systematically decreases as the water depth is increased.

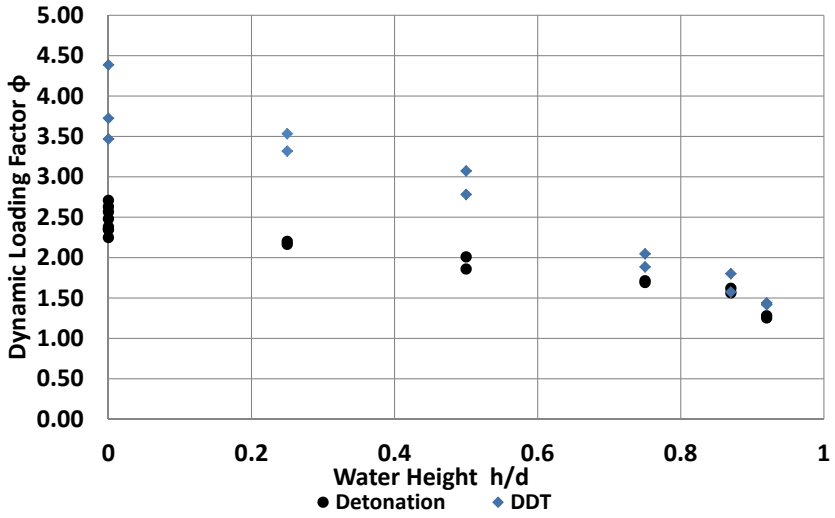

Figure 21: Dynamic loading factor vs. water depth for both detonations and DDT

Similar behavior is observed for DDT, with the exception that the peak strains are much higher at low water depths. The higher strains are expected since the DDT event produces peak pressures

which are much greater than those generated in a detonation. As the water depth increases, the high pressures produced by the DDT event decay more rapidly, and thus are confined to a smaller portion of the pipe. This causes the peak strains to be reduced. As h/d approaches 1, the effects of the DDT event are confined to such a small region that the strains respond as though to a detonation.

3.4 Heat Transfer

In Section 3.3, heat transfer was found to be responsible for a reduction in the peak strains. In the present section, the thermal insulation caused by the water is analyzed in more detail. Fig. 22 shows the strain traces over a 10 ms interval for a detonation over a water layer of depth h/d = 0.5. The gauges at the bottom of the tube remain centered at zero (or slightly negative), while the gauges at the side and top of the tube exhibit positive strains of about 30-40 $\mu\epsilon$. Thus although the thickness of the thermal layer is small (approximately $\sqrt{\kappa t} \sim 0.1$ mm, or about about 3% of the wall thickness), the resulting strains are the same order of magnitude as the dynamic strains.

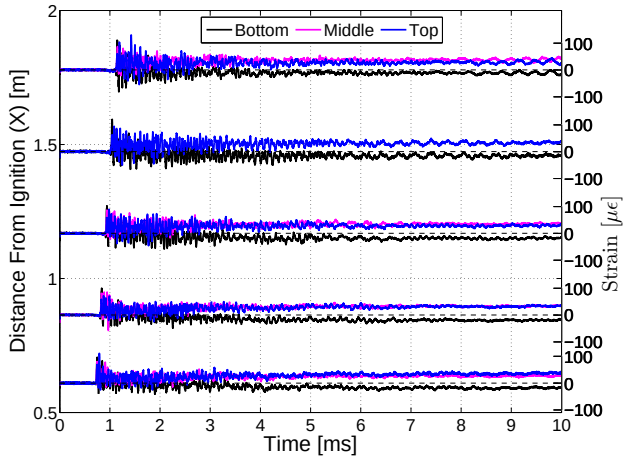

Figure 22: Long-time strain traces for a detonation with water depth h/d = 0.50

Finite element analysis was used to verify that the strain offset in Fig. 22 is indeed caused by heat transfer. A piecewise constant temperature distribution was assumed, with the thickness of the thermal layer assumed to be 0.1 mm, which was estimated using $\sqrt{\kappa t}$ with κ = 4.2x10^{-6} m^2/s and t = 5 ms. This temperature distribution is depicted in the inset of Fig. 23 (thermal layer thickness not to scale). The hot layer was taken to be 70° C hotter than the rest of the pipe, which was the temperature difference that best matched the experimental data; this temperature is presumably close to the average over the actual temperature distribution, which decays from the CJ temperature of about 3700 K at the surface of the wall to the ambient temperature in the interior of the pipe wall.

The finite element predictions are compared with experimental measurements in Fig. 23. The experimental data was compiled from the numerous shots with h/d = 0.50; in this series of shots the tube was incrementally rotated, so that hoop strain was measured at many angular positions around the pipe. In all cases, the data points plotted in Fig. 23 were taken at 100 ms, long after

the dynamic oscillations due to the detonation have died out. A sharp jump in hoop strain is observed where the water surface meets the pipe wall (θ = 90° and 270°), which is accompanied by a localized region of higher stress.

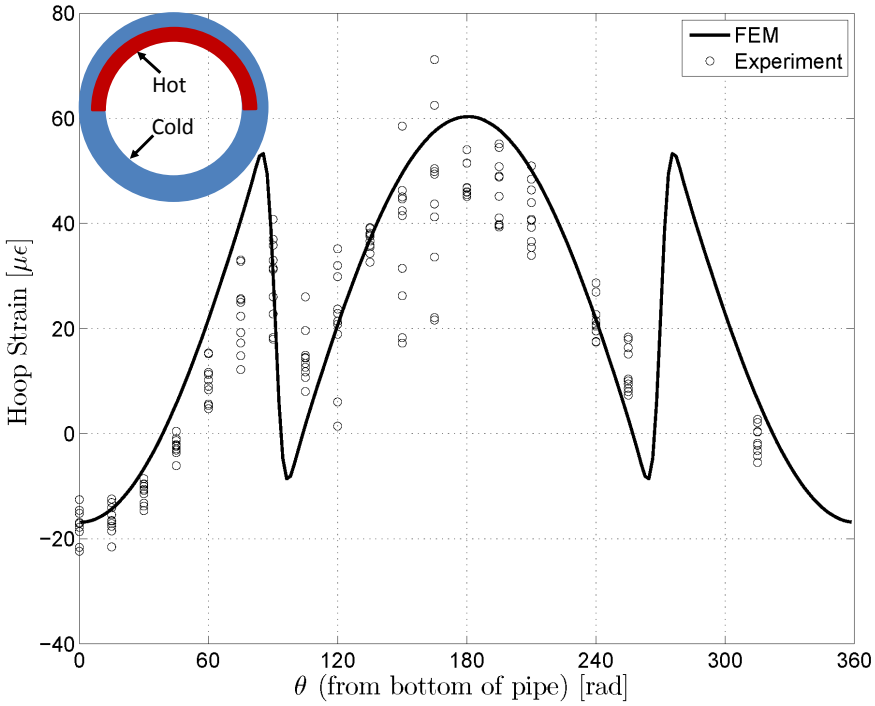

Figure 23: Comparison thermal hoop strains from experiments and finite element simulations. The finite element temperature distribution is shown inset (not to scale)

In industrial applications, the thermal hoop strains observed above would probably not produce large enough stresses to put the structural integrity of the pipe in jeopardy. Nevertheless, we have made two observations that have important implications in the design of industrial piping systems: thermal strains become non-negligible several milliseconds after the detonation passes, and the water insulates the bottom of the pipe. Although axial strains were not measured in this experiment, it is likely that the pipe experienced axial bending since the top of the tube expanded thermally while the bottom of the tube was insulated. In that case, the total bending moment (and hence bending stress) of the pipe would be proportional to its length. Thus a detonation over a water layer in a very long pipe could result in substantial bending stresses if the pipe is not properly restrained. Thus in addition to designing the piping system to withstand detonations, proper consideration of the thermal stresses must also be taken into account.

4 Conclusions

Detonations propagating over horizontal water layers in cylindrical pipes produce a train of oblique shock waves below the water which focus at the bottom of the pipe and yield peak pressures that are 4-6 times the peak detonation pressure. This pressure peak is of very short duration and confined to a small area, so that the overall pressure loading is only slightly increased. Meanwhile, the water damps the motion of the pipe both by adding mass and by insulating the bottom of the pipe, transferring energy to non-axisymmetric modes of vibration. As a result, the peak strains decrease with water depth despite the increase in peak pressure.

Detonations and DDT did not appear to be significantly affected by the presence of the water layer, though in all cases the gas layer thickness was greater than the detonation cell width. For DDT, transition distances were consistently between 30 and 60 cm, and no clear trend was found between transition distance and water depth.

References

R. Akbar and J. E. Shepherd. Detonation initiation and propagation within gas layers in water-filled piping. Technical Report FM2010-003, Graduate Aeronautical Laboratories California Institute of Technology, June 2010. Revised June 2010. 3, 6, 25, 26

W. Beltman and J.E. Shepherd. Linear elastic response of tubes to internal detonation loading. *Journal of Sound and Vibration*, 252(4), 2002. 30

G. Ben-Dor. *Shock Wave Reflection Phenomena*. Springer, 2 edition, 2007. 17

W.R. Benedick, R. Knystautas, and J.H. Lee. Dynamics of shock waves, explosions, and detonations. *Progress in Astronautics and Aeronautics*, 94:546–555, 1985. 22

N. P. Bitter and J. E. Shepherd. Detonation and transition to detonation in partially water-filled pipes. In *ASME Pressure Vessels and Piping Conference*. ASME, 2012. PVP2012-78539, July 15-19, 2012. Toronto, Ontario, Canada. 6, 11

Robert D. Blevins. *Formulas for Natural Frequency and Mode Shape*. Van Nostrand Reinhold Co., 1979. 27, 29

William E. Boyce and Richard C. DiPrima. *Elementary Differential Equations and Boundary Value Problems*. Wiley, 9th edition, 2009. 15

M. Kaneshige and J.E. Shepherd. Detonation database. Technical Report FM97-8, GALCIT, July 1997. 8, 25

L. Mahoney, J. Huckaby, S. Bryan, and G. Johnson. Overview of the flammability of gases generated in hanford waste tanks. Technical Report PNNL-13269, U.S. Department of Energy, July 2000. 6

B. Skews and H. Kleine. Flow features resulting from shock wave impact on a cylindrical cavity. *J. Fluid Mech*, 580:481–493, 2007. 17

A Shot List

Shot Number	Date	Water Filled?	Blockage Height [in]	h/d	Detonation or DDT	Fill Pressures [Torr]				Pre-Shot Temp [C]	Mole Fractions		Comments
						H2	O2	Total Gas	Total w/Liquid		H2	O2	
1	8/16/2011	No	1	0.00	Detonation	500.8	249.9	750.7	750.7	24.0	66.71%	33.29%	
2	8/23/2011	No	1	0.00	Detonation	500.5	249.7	750.2	750.2	24.6	66.72%	33.28%	6 strain gauges added at the reflecting end of the Tube
3	8/24/2011	Yes	1	0.50	Detonation	322.2	161.1	483.3	750.1	26.7	66.67%	33.33%	
4	8/25/2011	Yes	1	0.50	Detonation	322.1	161.0	483.1	749.9	24.3	66.67%	33.33%	
5	8/29/2011	No	0.5	0.00	Detonation	500.6	249.4	750.0	750.0	25.5	66.75%	33.25%	
6	8/29/2011	Yes	0.5	0.25	Detonation	408.6	204.3	612.9	752.1	27.6	66.67%	33.33%	
7	8/30/2011	No	0.5	0.00	Detonation	501.1	248.9	750.0	750.0	25.9	66.81%	33.19%	
8	8/31/2011	Yes	0.5	0.25	Detonation	408.2	204.5	612.7	750.1	25.3	66.62%	33.38%	
9	9/1/2011	Yes	1.5	0.75	Detonation	218.7	109.7	328.4	750.0	27.6	66.60%	33.40%	
10	9/6/2011	No	1.5	0.00	Detonation	500.5	249.6	750.1	750.1	24.7	66.72%	33.28%	
11	9/6/2011	No	1.5	0.00	Detonation	499.8	250.2	750.0	750.1	26.6	66.64%	33.36%	
12	9/6/2011	Yes	1.5	0.75	Detonation	218.8	109.7	328.5	750.0	27.8	66.61%	33.39%	
13	9/8/2011	No	1	0.00	DDT	500.0	250.1	750.1	750.1	26.0	66.66%	33.34%	No Shelkin in Tube; Ignition at East End
14	9/8/2011	No	1	0.00	DDT	500.0	250.0	750.0	750.0	26.6	66.67%	33.33%	No Shelkin in Tube; Ignition at East End
15	9/8/2011	Yes	1	0.50	DDT	336.5	168.0	504.5	750.0	27.2	66.70%	33.30%	No Shelkin in Tube; Ignition at East End
16	9/12/2011	Yes	1	0.50	DDT	336.3	168.3	504.6	750.0	26.0	66.65%	33.35%	No Shelkin in Tube; Ignition at East End
17	9/12/2011	No	1	0.00	DDT	499.8	250.2	750.0	750.0	26.1	66.64%	33.36%	Ignition at the water-fill end of the tube (spark plug in P9 Port)
18	9/12/2011	No	1	0.00	DDT	499.8	250.2	750.0	750.0	27.5	66.64%	33.36%	Ignition at the water-fill end of the tube (spark plug in P9 Port)
19	9/13/2011	Yes	1	0.50	DDT	336.2	168.3	504.5	750.0	24.8	66.64%	33.36%	Ignition at the water-fill end of the tube (spark plug in P9 Port)
20	9/13/2011	Yes	1	0.50	DDT	336.2	168.4	504.6	750.4	27.8	66.63%	33.37%	Ignition at the water-fill end of the tube (spark plug in P9 Port)
21	9/14/2011	No	1	0.00	Detonation	500.0	250.0	750.0	750.0	26.5	66.67%	33.33%	Rotated 45 Degrees
22	9/16/2011	No	1	0.00	Detonation	500.0	250.0	750.0	750.0	26.2	66.67%	33.33%	Rotated 45 Degrees
23	9/16/2011	Yes	1	0.50	Detonation	336.3	168.3	504.6	751.2	26.8	66.65%	33.35%	Rotated 45 Degrees
24	9/20/2011	Yes	1	0.50	Detonation	336.4	168.1	504.5	751.6	25.3	66.68%	33.32%	Rotated 45 Degrees
25	9/23/2011	No	1	0.00	Detonation	500.2	249.8	750.0	751.1	26.6	66.69%	33.31%	Rotated 15 Degrees
26	9/23/2011	No	1	0.00	Detonation	500.0	250.0	750.0	746.8	26.8	66.67%	33.33%	Rotated 15 Degrees
27	9/26/2011	Yes	1	0.50	Detonation	340.9	170.6	511.5	749.9	26.4	66.65%	33.35%	Rotated 15 Degrees
28	9/26/2011	Yes	1	0.50	Detonation	341.0	170.6	511.6	750.0	25.3	66.65%	33.35%	Rotated 15 Degrees
29	9/27/2011	No	1	0.00	Detonation	500.3	249.9	750.2	749.5	26.4	66.69%	33.31%	Rotated 30 Degrees
30	9/28/2011	No	1	0.00	Detonation	500.0	250.0	750.0	751.2	26.3	66.67%	33.33%	Rotated 30 Degrees; Gauge P8 lost protective coating
31	9/28/2011	Yes	1	0.50	Detonation	341.1	170.4	511.5	750.0	26.9	66.69%	33.31%	Rotated 30 Degrees
32	9/30/2011	Yes	1	0.50	Detonation	341.1	170.4	511.5	750.1	26.3	66.69%	33.31%	Rotated 30 Degrees
33	10/5/2011	No	1	0.00	Detonation	500.4	249.6	750.0	750.1	26.1	66.72%	33.28%	Rotated 60 Degrees; Gauge P8 lost protective coating
34	10/5/2011	No	1	0.00	Detonation	500.3	249.7	750.0	750.5	26.9	66.71%	33.29%	Rotated 60 Degrees, Gauge P8 Lost Protective Coating
35	10/6/2011	Yes	1	0.50	Detonation	340.9	170.8	511.7	750.1	26.0	66.62%	33.38%	Rotated 60 Degrees
36	10/6/2011	Yes	1	0.50	Detonation	341.3	170.3	511.6	750.2	24.6	66.71%	33.29%	Rotated 60 Degrees
37	10/7/2011	No	1	0.00	Detonation	500.0	250.0	750.0	747.6	26.2	66.67%	33.33%	Rotated 75 Degrees; Gauge P8 no protective coating
38	10/10/2011	No	1	0.00	Detonation	500.0	250.0	750.0	747.4	25.8	66.67%	33.33%	Rotated 75 Degrees; Gauge P8 no protective coating
39	10/12/2011	Yes	1	0.50	Detonation	341.0	170.6	511.6	750.2	26.1	66.65%	33.35%	Rotated 75 Degrees;
40	10/12/2011	Yes	1	0.50	Detonation	341.0	173.5	514.5	750.2	24.8	66.28%	33.72%	Rotated 75 Degrees
41	10/12/2011	Yes	1.5	0.75	DDT	218.9	109.5	328.4	800.3	25.8	66.66%	33.34%	Ignition at the water-fill end of the tube (spark plug in P9 Port)
42	10/13/2011	Yes	1.5	0.75	DDT	218.8	109.6	328.4	750.0	26.0	66.63%	33.37%	Ignition at the water-fill end of the tube (spark plug in P9 Port)
43	10/14/2011	Yes	None	0.50	DDT	283.5	141.9	425.4	750.0	26.2	66.64%	33.36%	No Blockage, Half Full (1") of Water, Ignition in P9
44	11/23/2011	No	None	0.00	Detonation	499.8	250.0	749.8	747.1	26.2	66.66%	33.34%	Rubber Sheet covering lower half of tube (covers P3 and S13-18)
45	11/23/2011	No	None	0.00	Detonation	499.8	250.2	750.0	750.8	26.9	66.64%	33.36%	Rubber Sheet covering lower half of tube (covers P3 and S13-18)
46	11/23/2011	No	None	0.00	Detonation	500.0	250.0	750.0	749.6	27.1	66.67%	33.33%	Baseline shot with no blockage, no water.
47	11/30/2011	Yes	None	0.65	DDT	147.2	73.7	220.9	750.7	25.5	66.64%	33.36%	No Blockage, h/d<0.75, Ignition at P9
48	11/30/2011	Yes	None	0.75	DDT	100.5	50.1	150.6	752.8	25.4	66.73%	33.27%	No Blockage, h/d=0.75, Ignition at P9
49	12/1/2011	Yes	None	0.75	DDT	80.1	40.0	120.1	750.7	25.4	66.69%	33.31%	No Blockage, h/d=0.75, Ignition at P9
50	12/3/2011	Yes	None	0.83	DDT	60.0	30.0	90.0	749.4	25.0	66.67%	33.33%	No Blockage, h/d=0.83 as measured, Ignition at P9,
51	12/6/2011	Yes	None	0.78	DDT	80.0	40.1	120.1	750.0	25.9	66.61%	33.39%	No Blockage, h/d=0.78, Ignition at East end above water
52	12/7/2011	Yes	None	0.78	DDT	80.1	39.9	120.0	750.3	25.4	66.75%	33.25%	No Blockage, h/d=0.78, Ignition at East end above water
53	12/8/2011	Yes	None	0.81	DDT	60.0	30.2	90.2	750.0	29.6	66.52%	33.48%	No Blockage, h/d=0.81, Ignition at East end above water
54	12/13/2011	No	1.75	0.00	Detonation	500.1	250.0	750.1	748.6	24.4	66.67%	33.33%	
55	12/13/2011	No	1.75	0.00	Detonation	500.1	250.0	750.1	747.2	26.6	66.67%	33.33%	
56	12/13/2011	Yes	1.75	0.88	Detonation	180.1	93.0	273.1	750.1	26.8	65.95%	34.05%	
57	12/13/2011	Yes	1.75	0.88	Detonation	180.2	89.9	270.1	750.5	25.8	66.72%	33.28%	
58	12/14/2011	Yes	1.75	0.88	DDT	180.2	90.2	270.4	749.9	26.1	66.64%	33.36%	
59	12/14/2011	Yes	1.75	0.88	DDT	179.9	90.0	269.9	749.8	24.9	66.65%	33.35%	
60	12/15/2011	No	1.875	0.00	Detonation	500.4	249.6	750.0	748.2	25.0	66.72%	33.28%	
61	12/15/2011	No	1.875	0.00	Detonation	500.0	250.1	750.1	751.1	25.0	66.66%	33.34%	
62	12/15/2011	Yes	1.875	0.94	Detonation	170.0	84.0	254.0	750.4	26.3	66.93%	33.07%	
63	12/16/2011	Yes	1.875	0.94	Detonation	170.2	83.9	254.1	750.0	25.3	66.98%	33.02%	
64	12/16/2011	Yes	1.875	0.94	DDT	168.8	85.3	254.1	750.5	25.6	66.43%	33.57%	
65	12/17/2011	Yes	1.875	0.94	DDT	170.0	84.1	254.1	750.1	25.6	66.90%	33.10%	
66	12/22/2011	No	None	0.00	DDT	500.0	249.9	749.9	748.5	25.6	66.68%	33.32%	
67	12/22/2011	No	None	0.00	DDT	500.1	249.9	750.0	747.3	27.0	66.68%	33.32%	
68	12/22/2011	Yes	None	0.44	DDT	272.2	135.8	408.0	750.0	26.9	66.72%	33.28%	DDT From East End Above Water
69	1/10/2012	Yes	0.5	0.25	DDT	403.8	201.9	605.7	750.8	25.7	66.67%	33.33%	DDT with ignition at P9
70	1/10/2012	Yes	0.5	0.25	DDT	403.9	201.9	605.8	751.2	25.6	66.67%	33.33%	DDT with ignition at P9
71	1/11/2012	No	0.5	0.00	DDT	500.0	249.9	749.9	747.6	25.4	66.68%	33.32%	DDT with ignition at P9
72	1/11/2012	No	0.5	0.00	DDT	500.2	249.8	750.0	751.1	26.3	66.69%	33.31%	DDT with ignition at P9
73	1/11/2012	Yes	0.5	0.25	DDT	322.0	161.1	483.1	749.9	26.4	66.65%	33.35%	
74	3/14/2012	No	None	0.00	Detonation	498.8	251.2	750.0	747.4	26.0	66.51%	33.49%	
75	3/14/2012	No	None	0.00	Detonation	500.2	249.8	750.0			66.69%	33.31%	
				0.00									

Figure 24: Shot List

B Pressure Traces

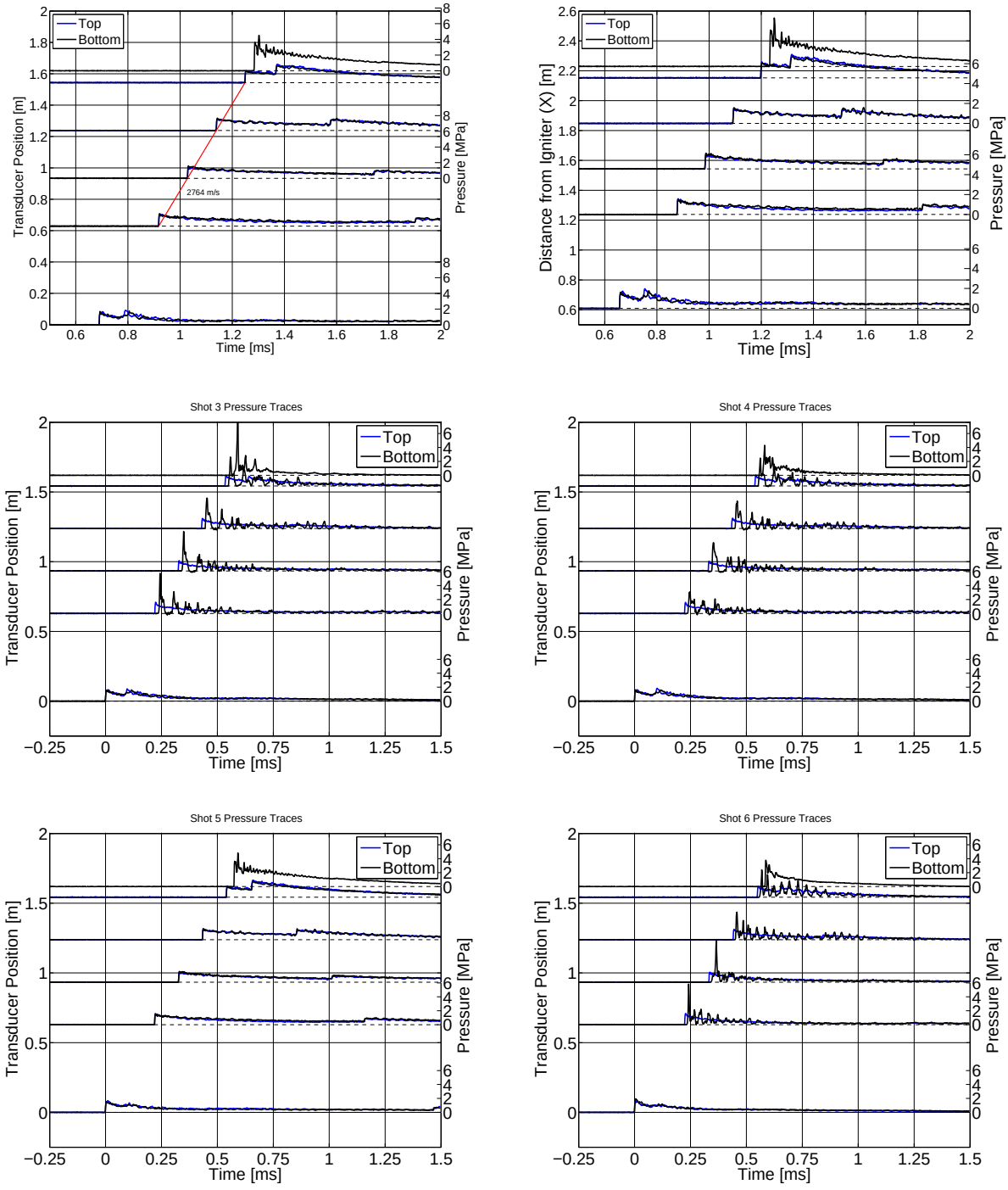

Figure 25: Pressure Traces for shots 1-6

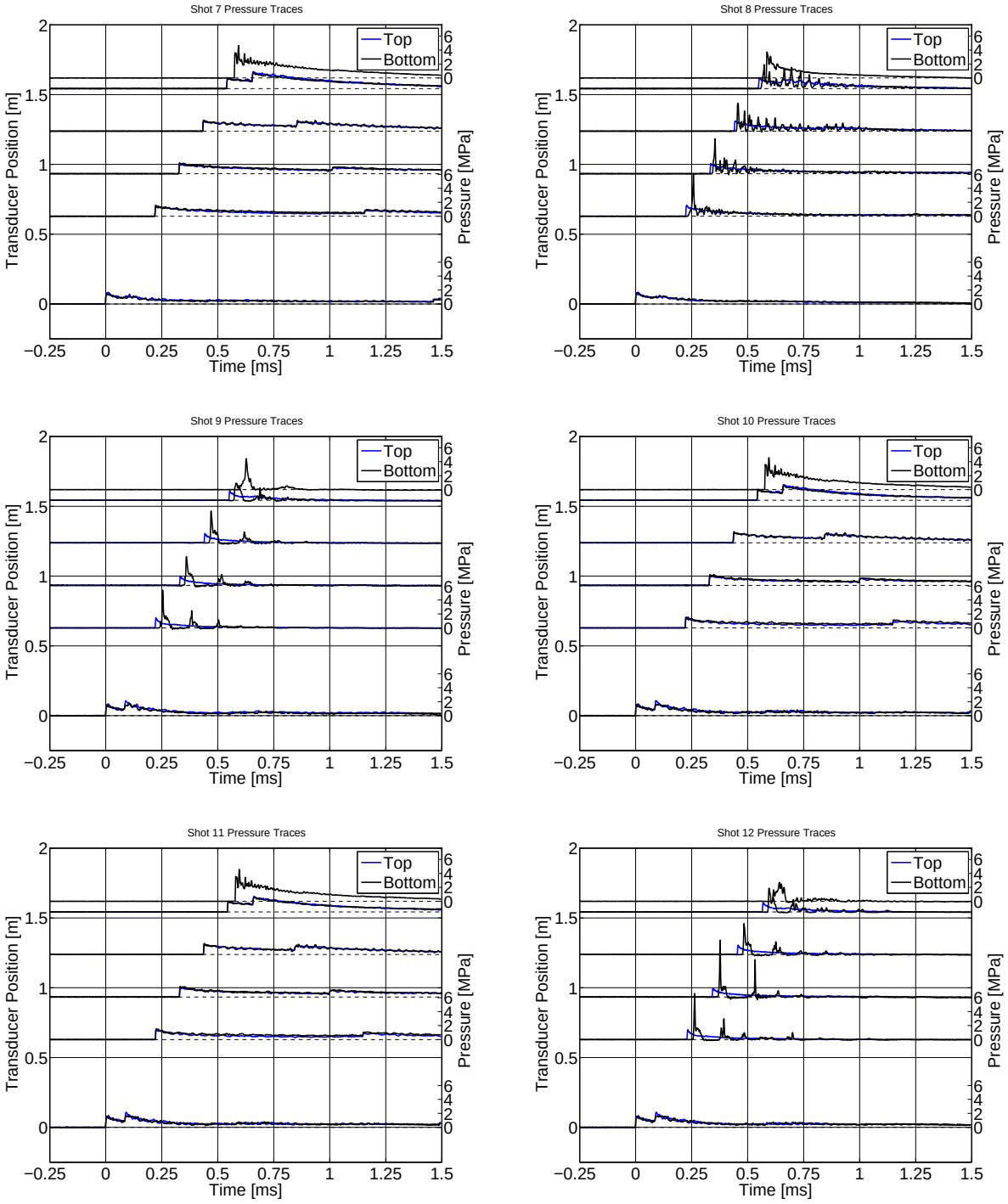

Figure 26: Pressure Traces for shots 7-12

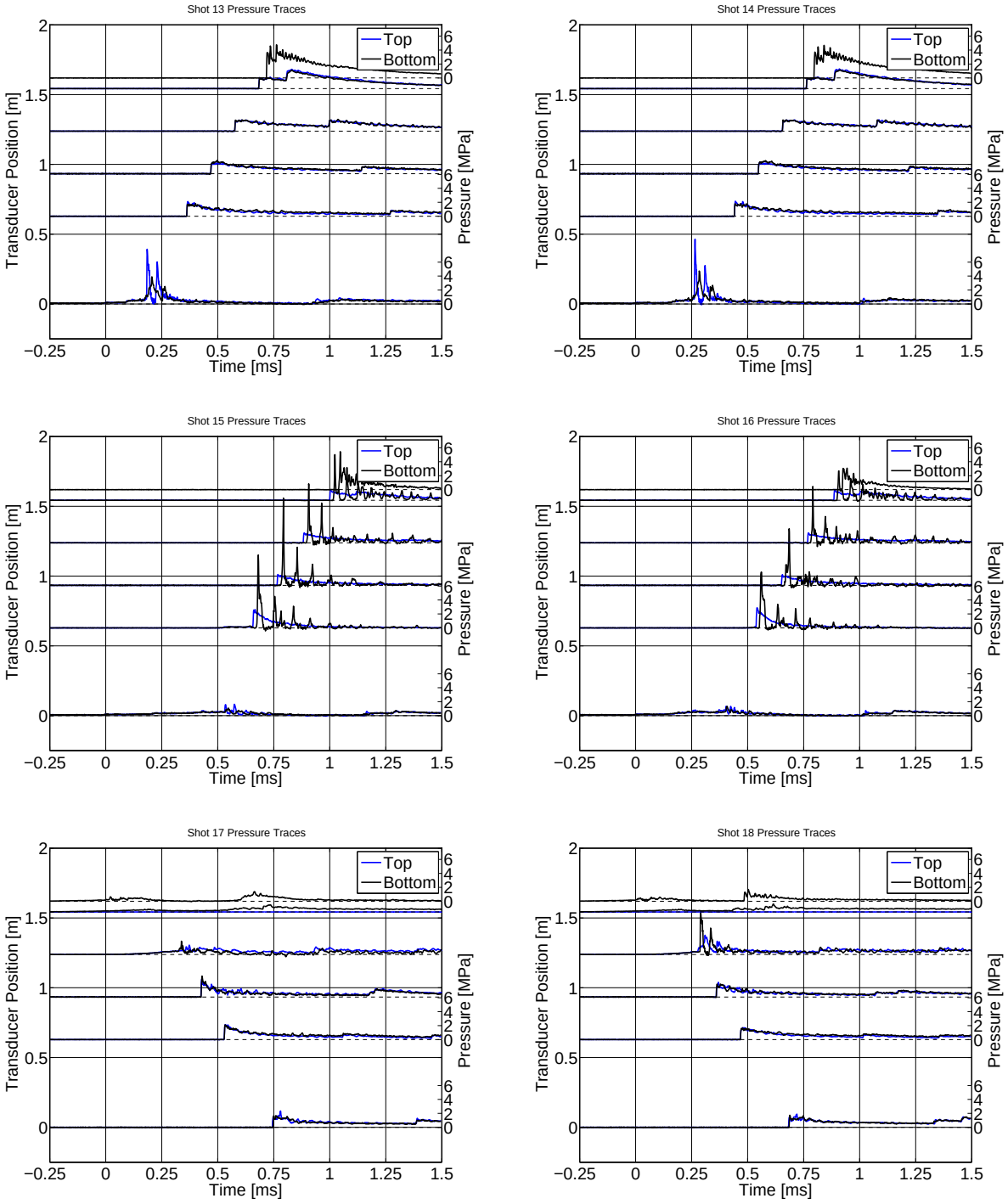

Figure 27: Pressure Traces for shots 13-18

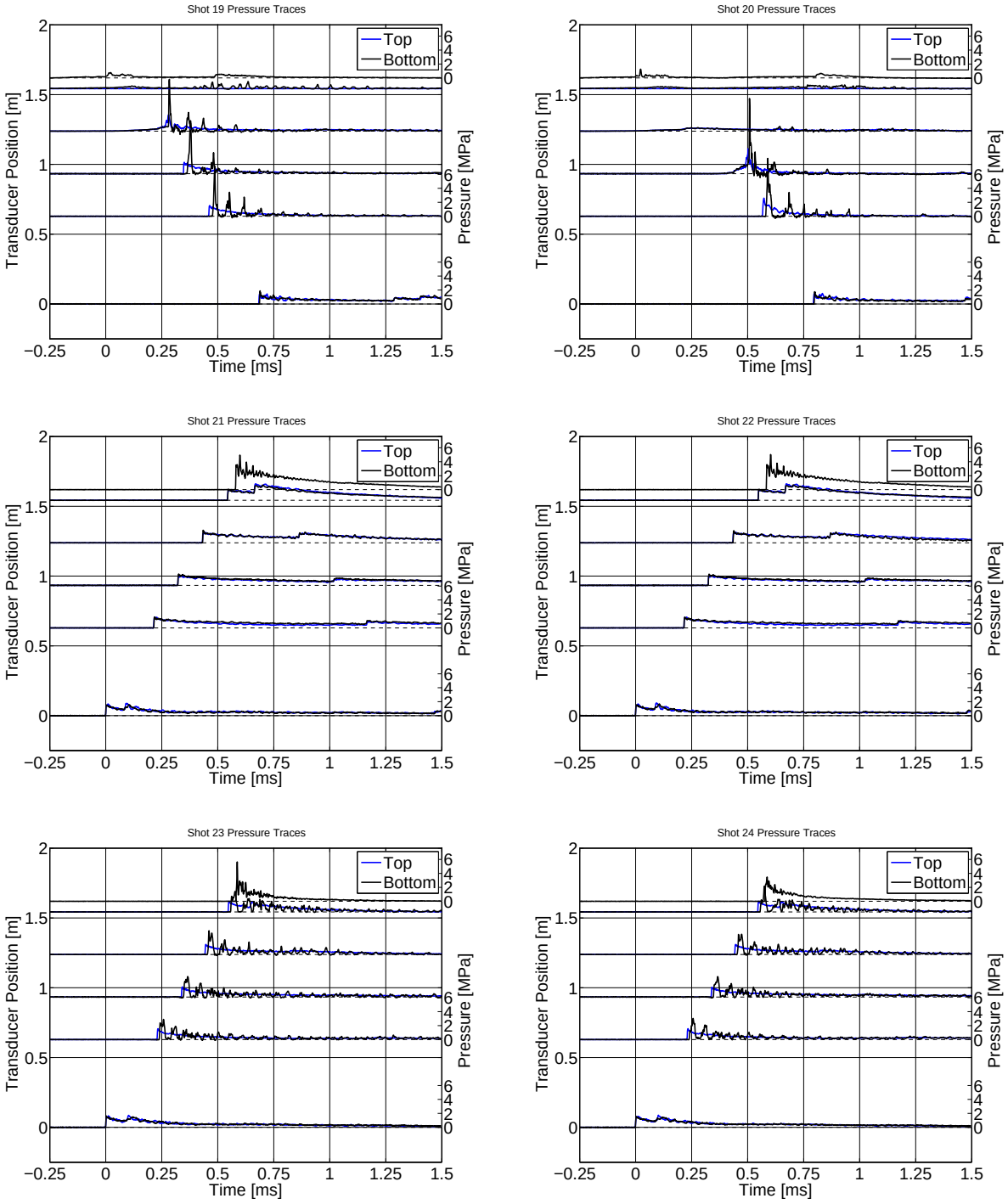

Figure 28: Pressure Traces for shots 19-24

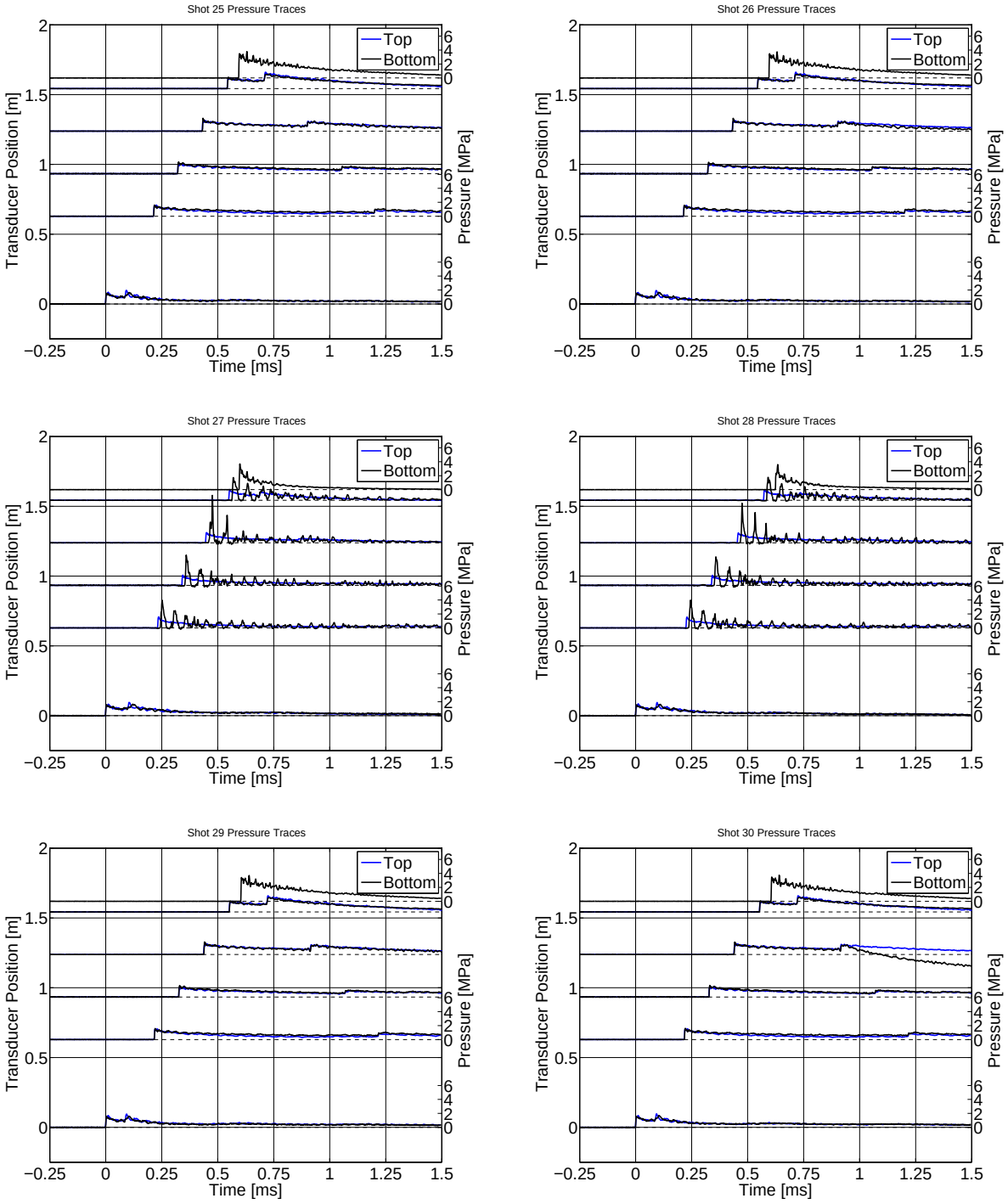

Figure 29: Pressure Traces for shots 25-30

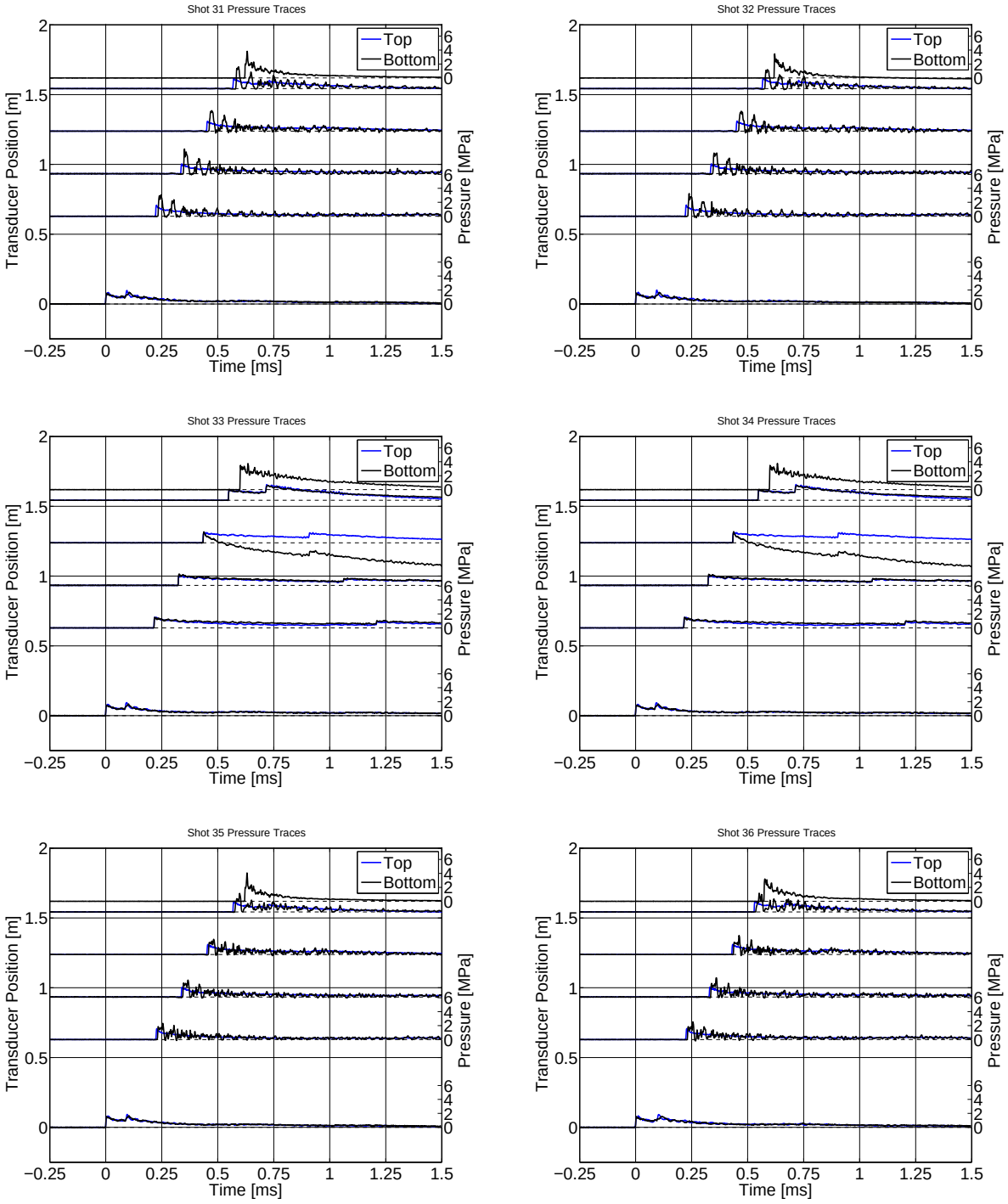

Figure 30: Pressure Traces for shots 31-36

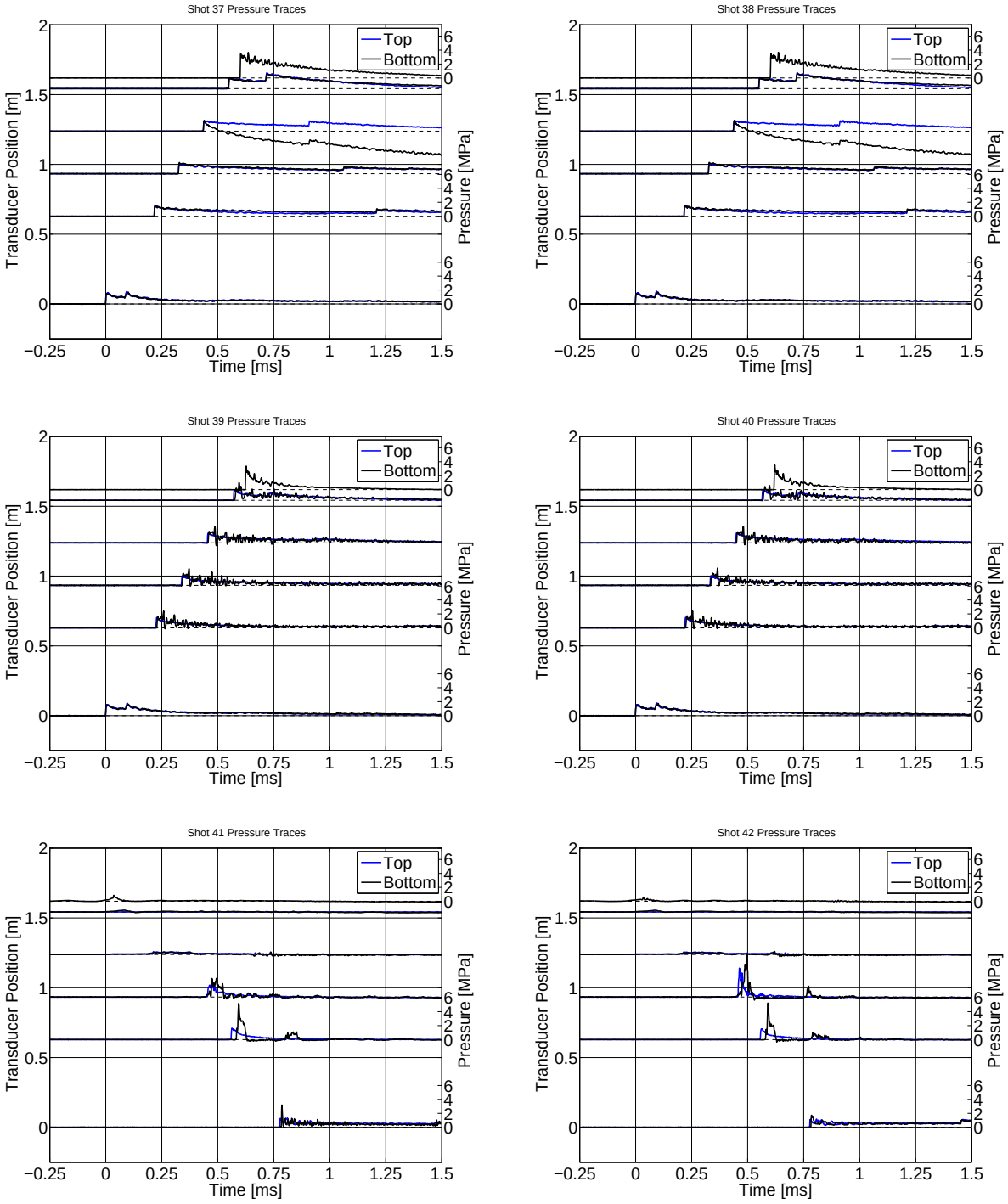

Figure 31: Pressure Traces for shots 37-42

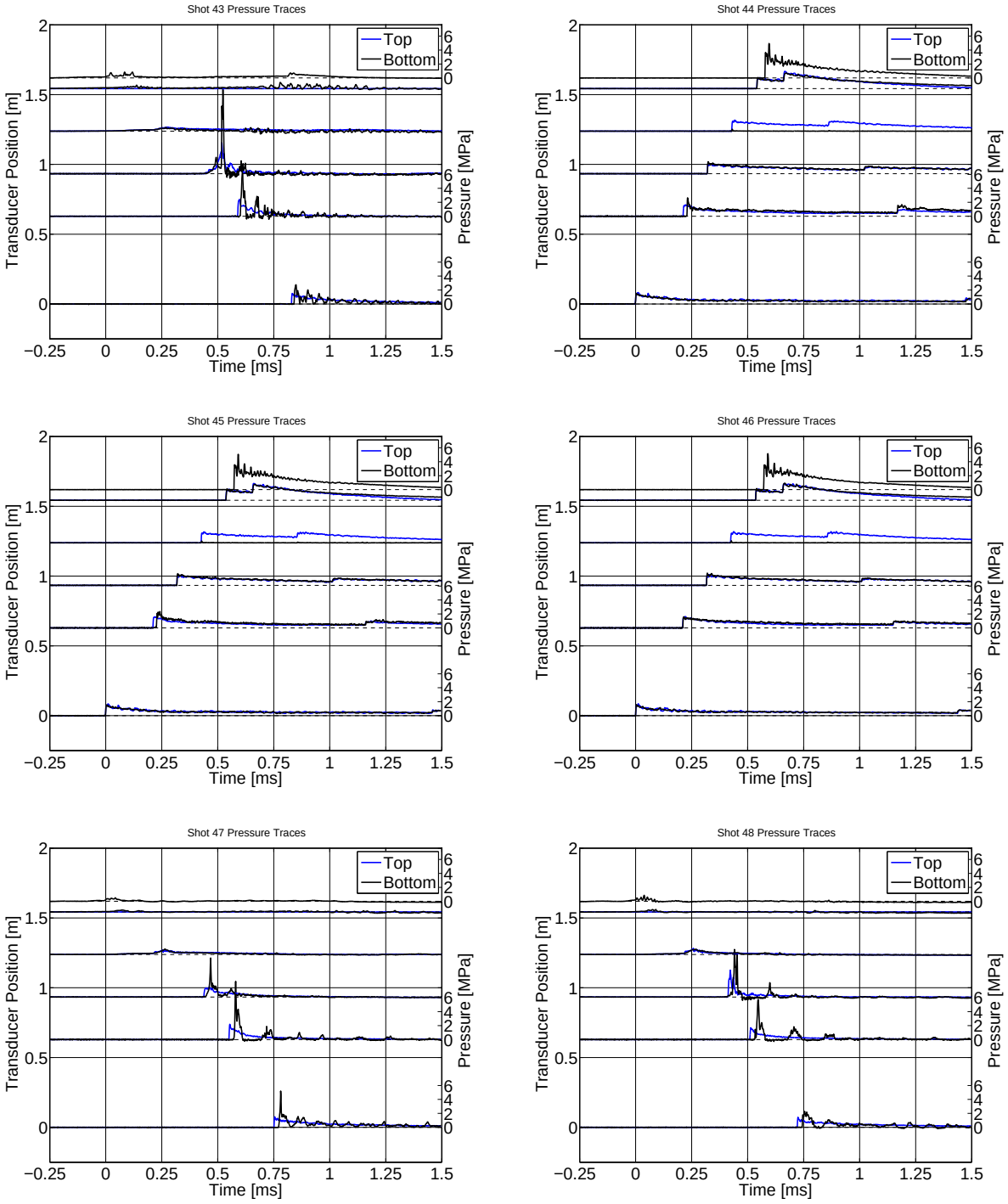

Figure 32: Pressure Traces for shots 43-48

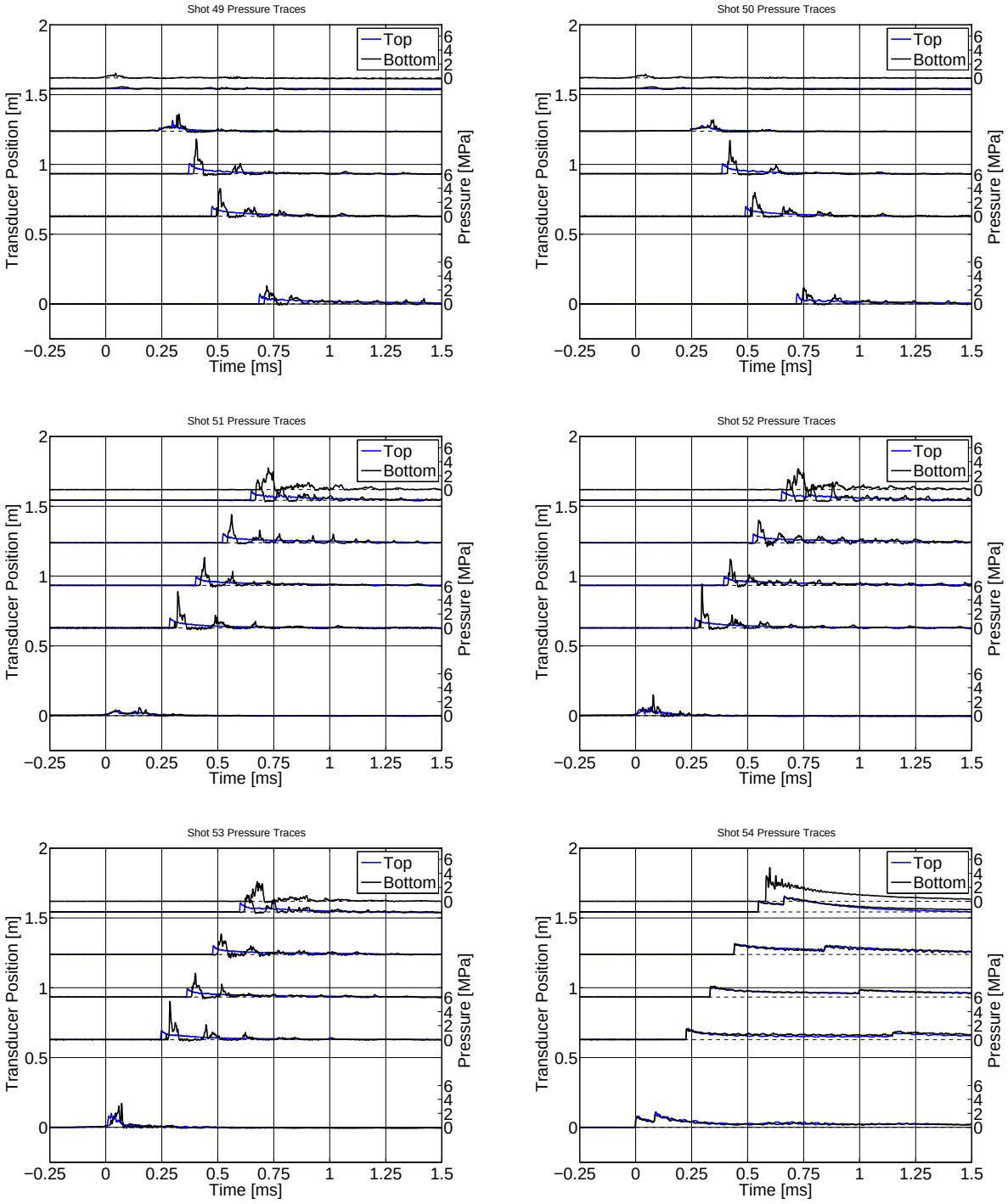

Figure 33: Pressure Traces for shots 49-54

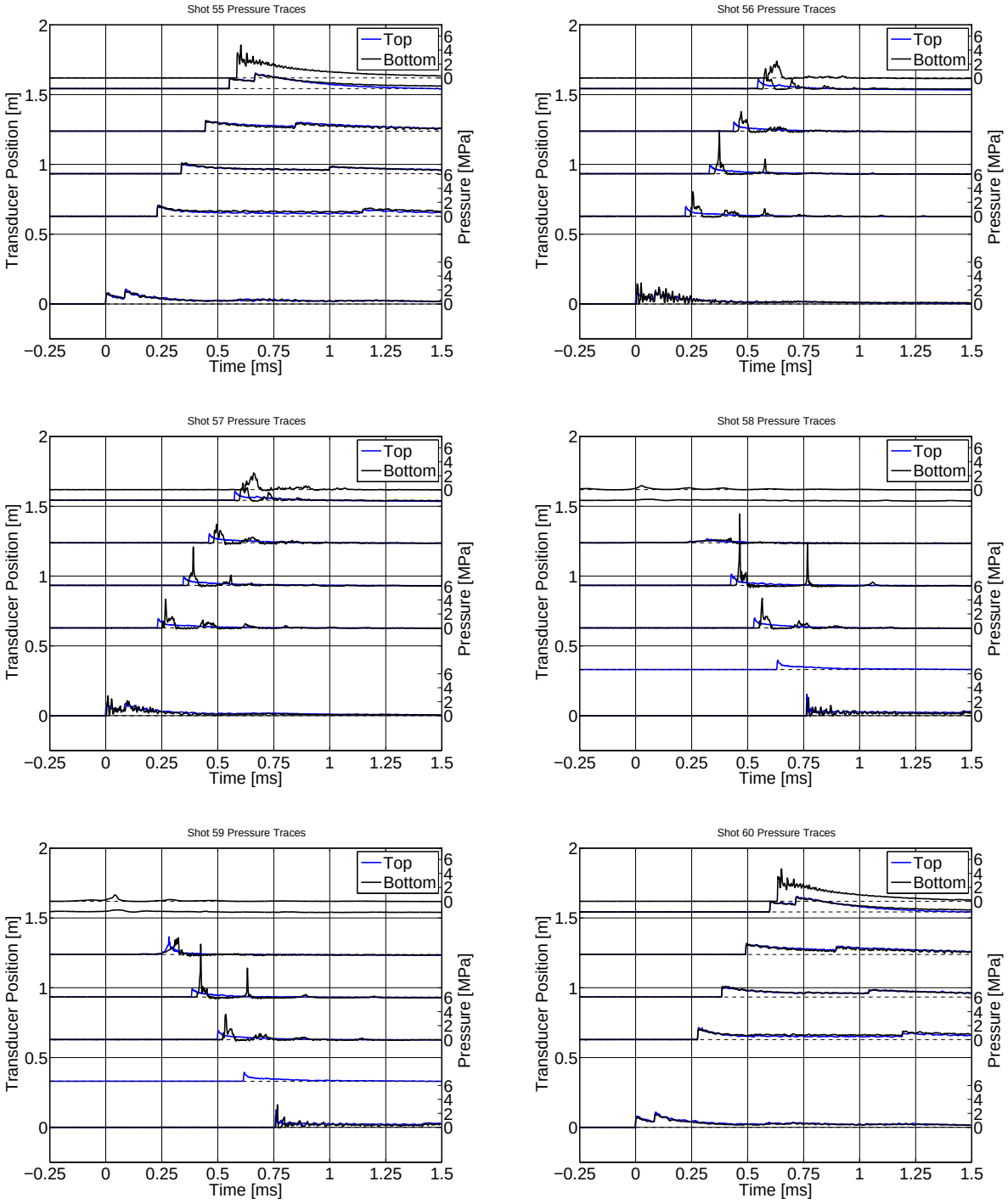

Figure 34: Pressure Traces for shots 55-60

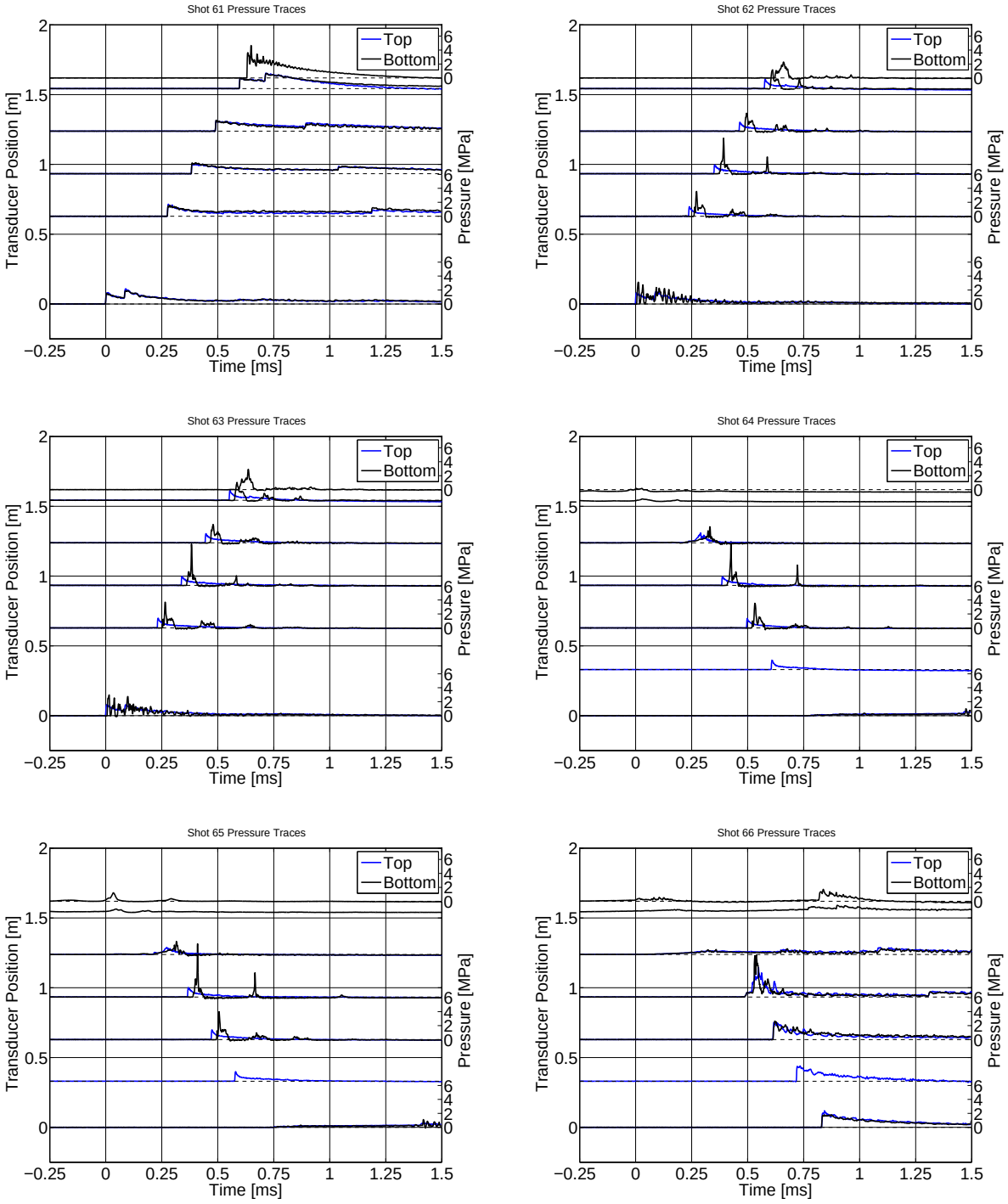

Figure 35: Pressure Traces for shots 61-66

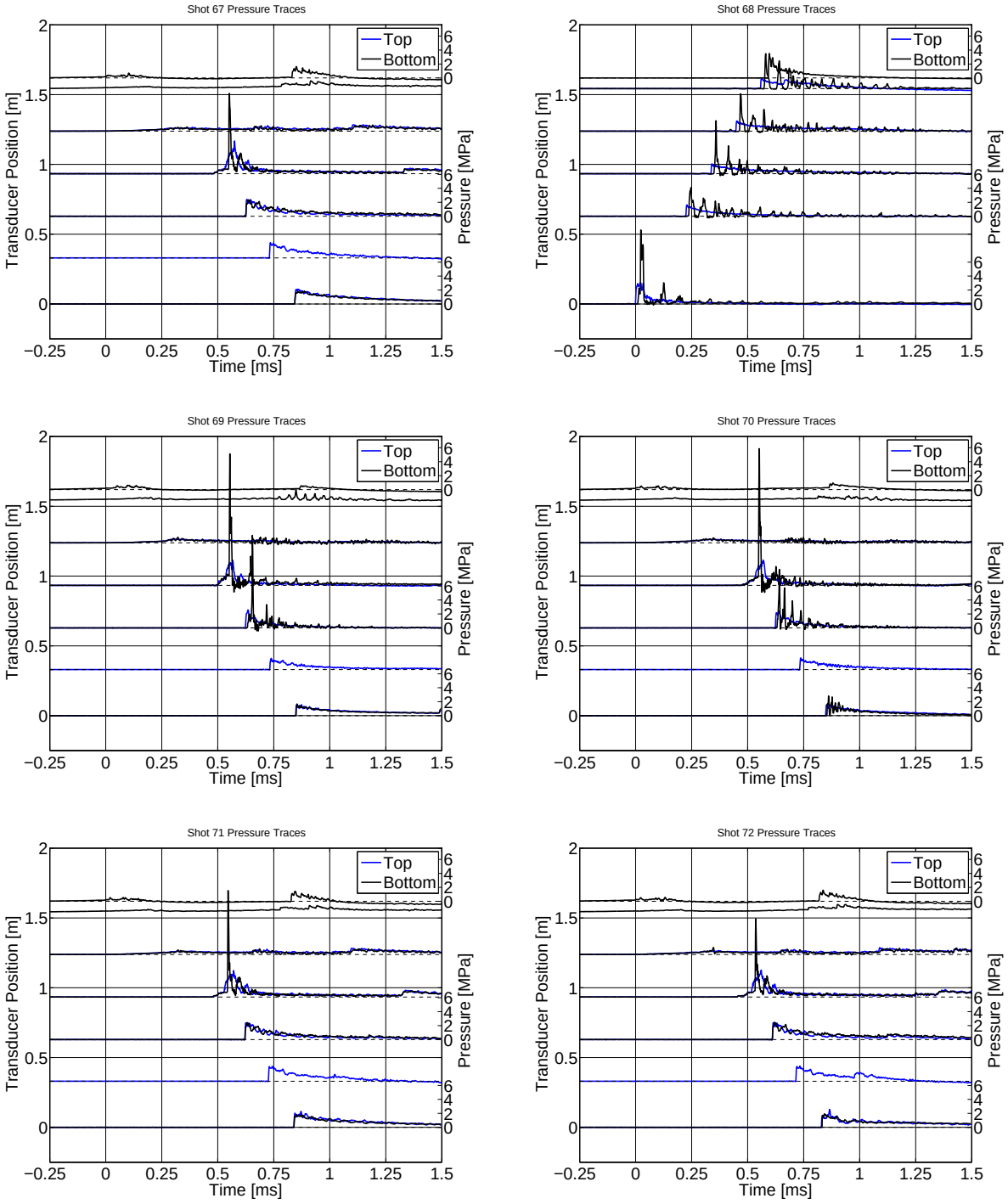

Figure 36: Pressure Traces for shots 67-72

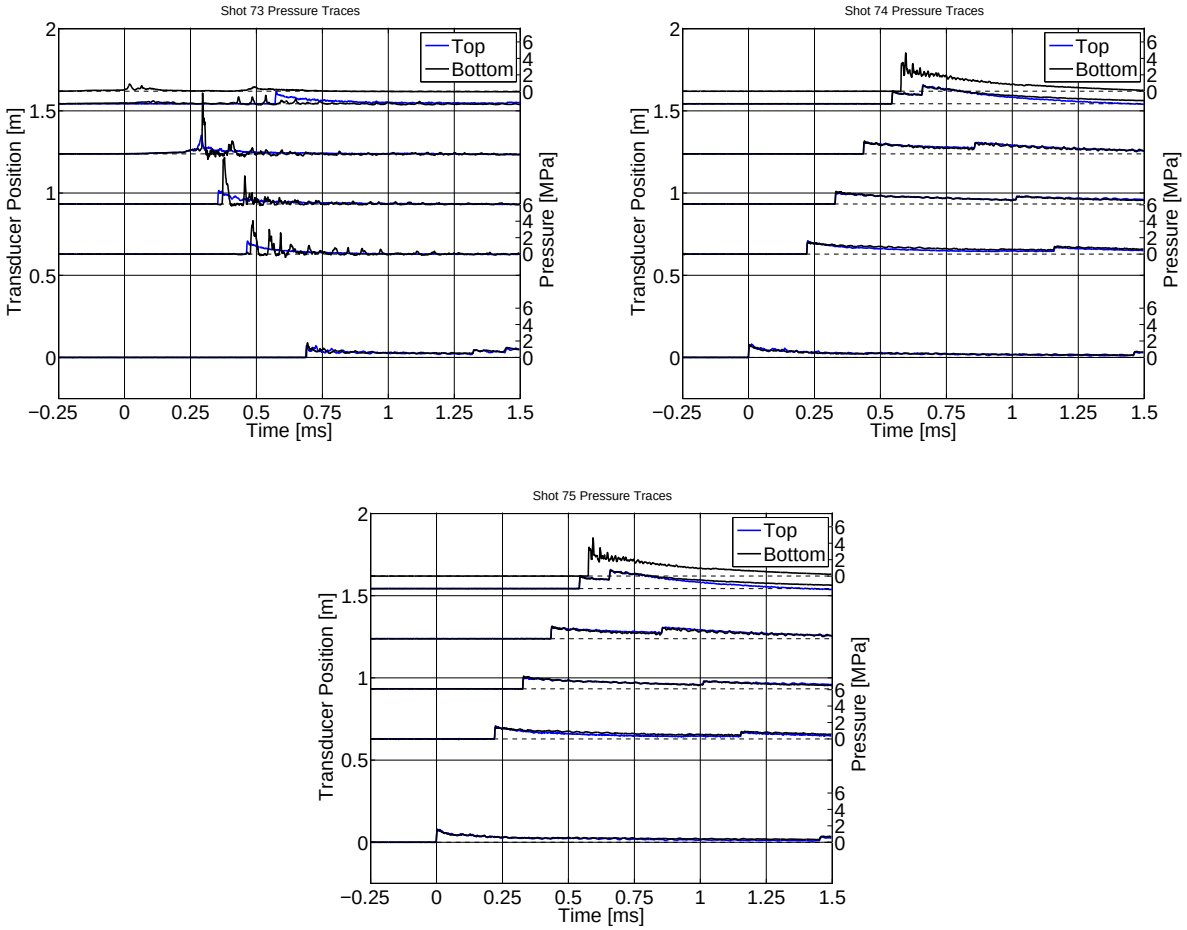

Figure 37: Pressure Traces for shots 72-75

C Strain Traces

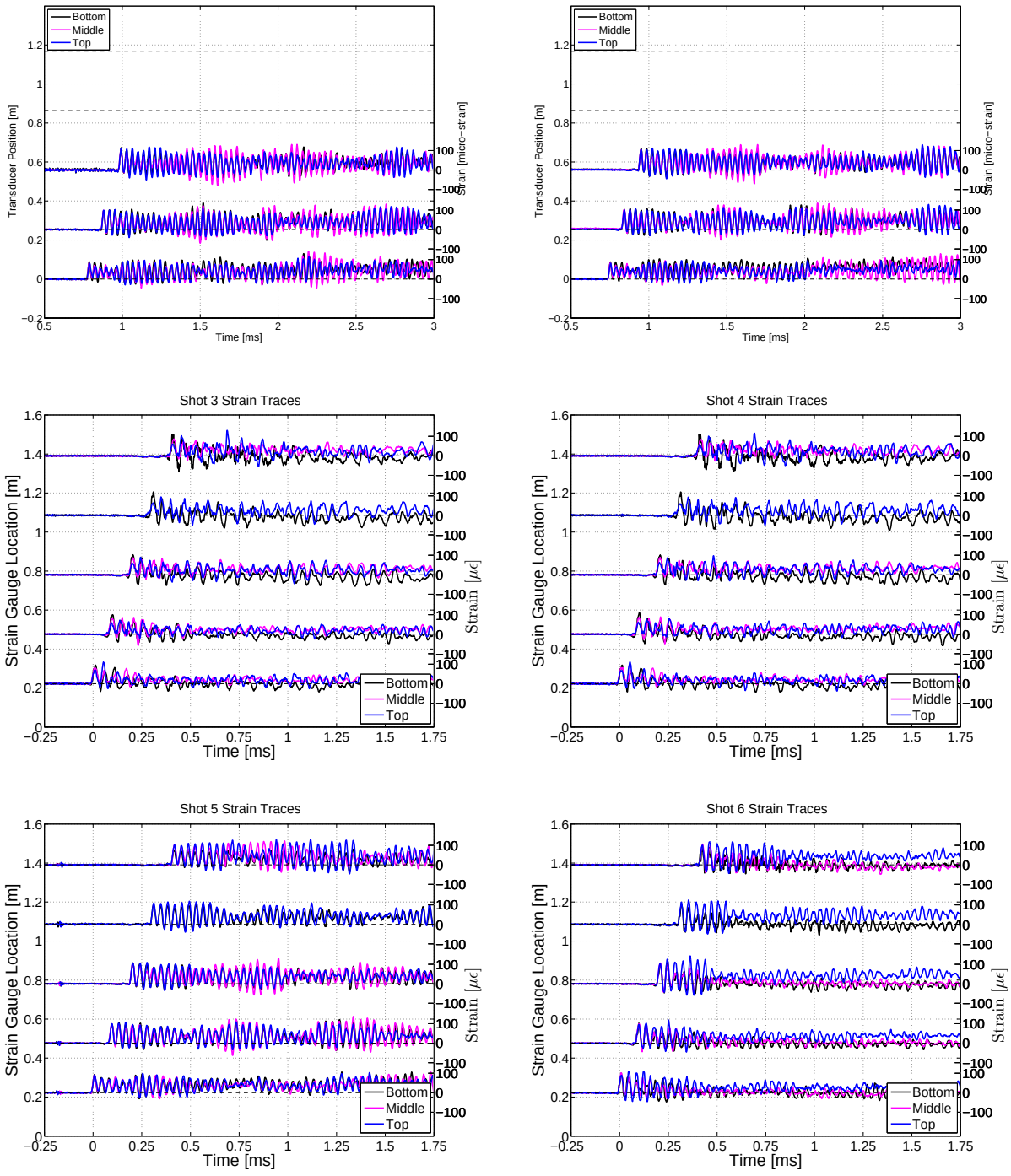

Figure 38: Strain Traces for shots 1-6

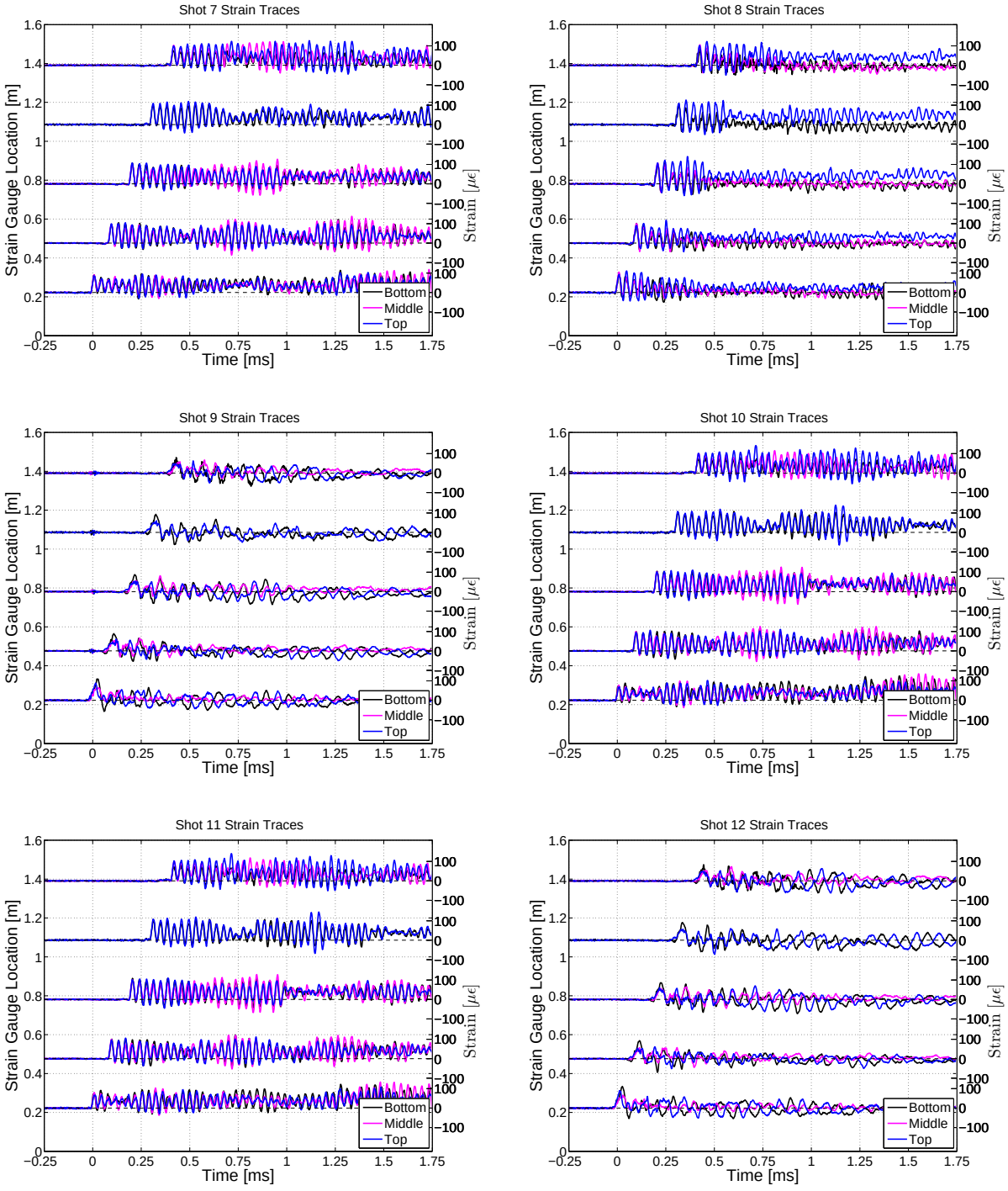

Figure 39: Strain Traces for shots 7-12

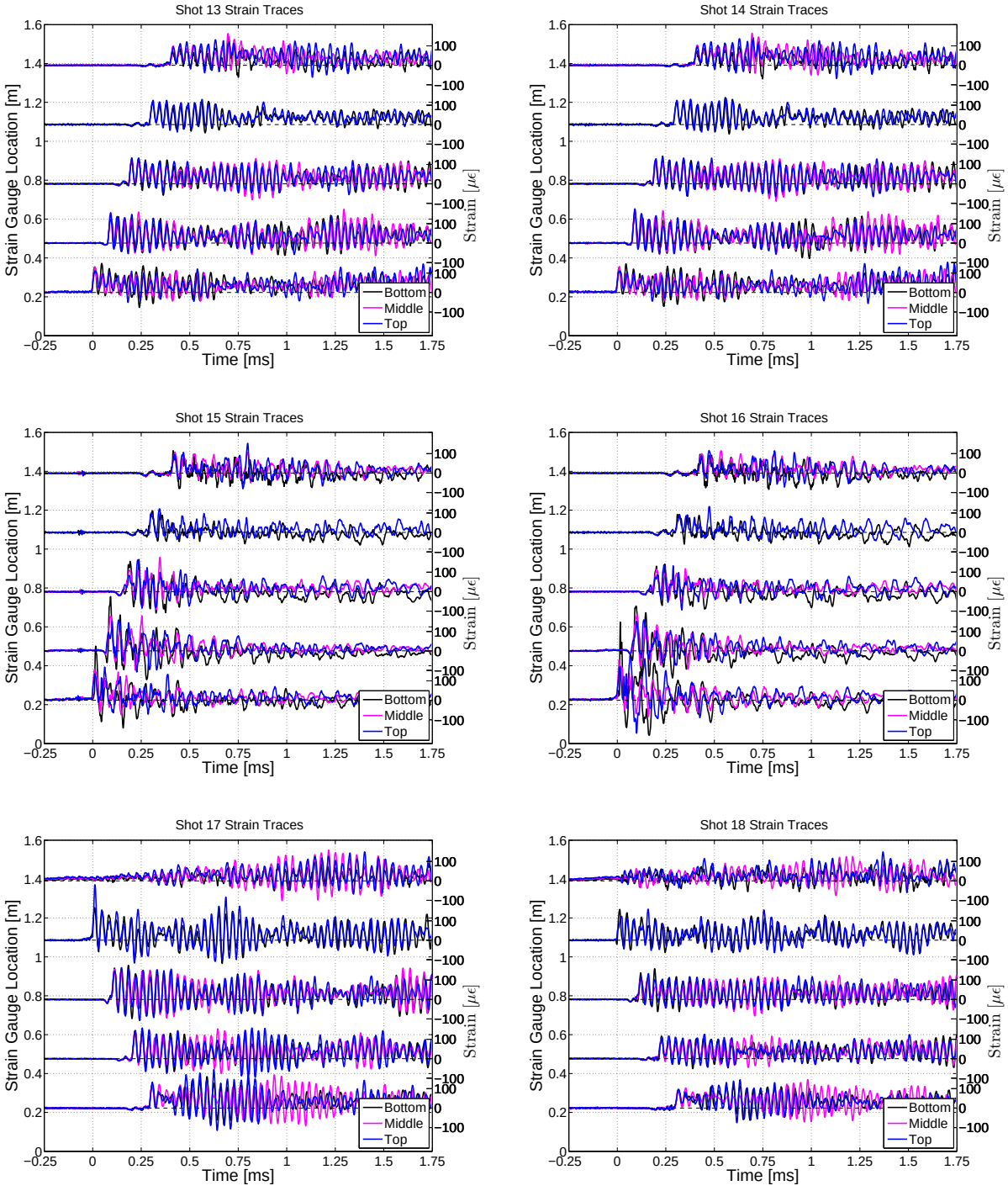

Figure 40: Strain Traces for shots 13-18

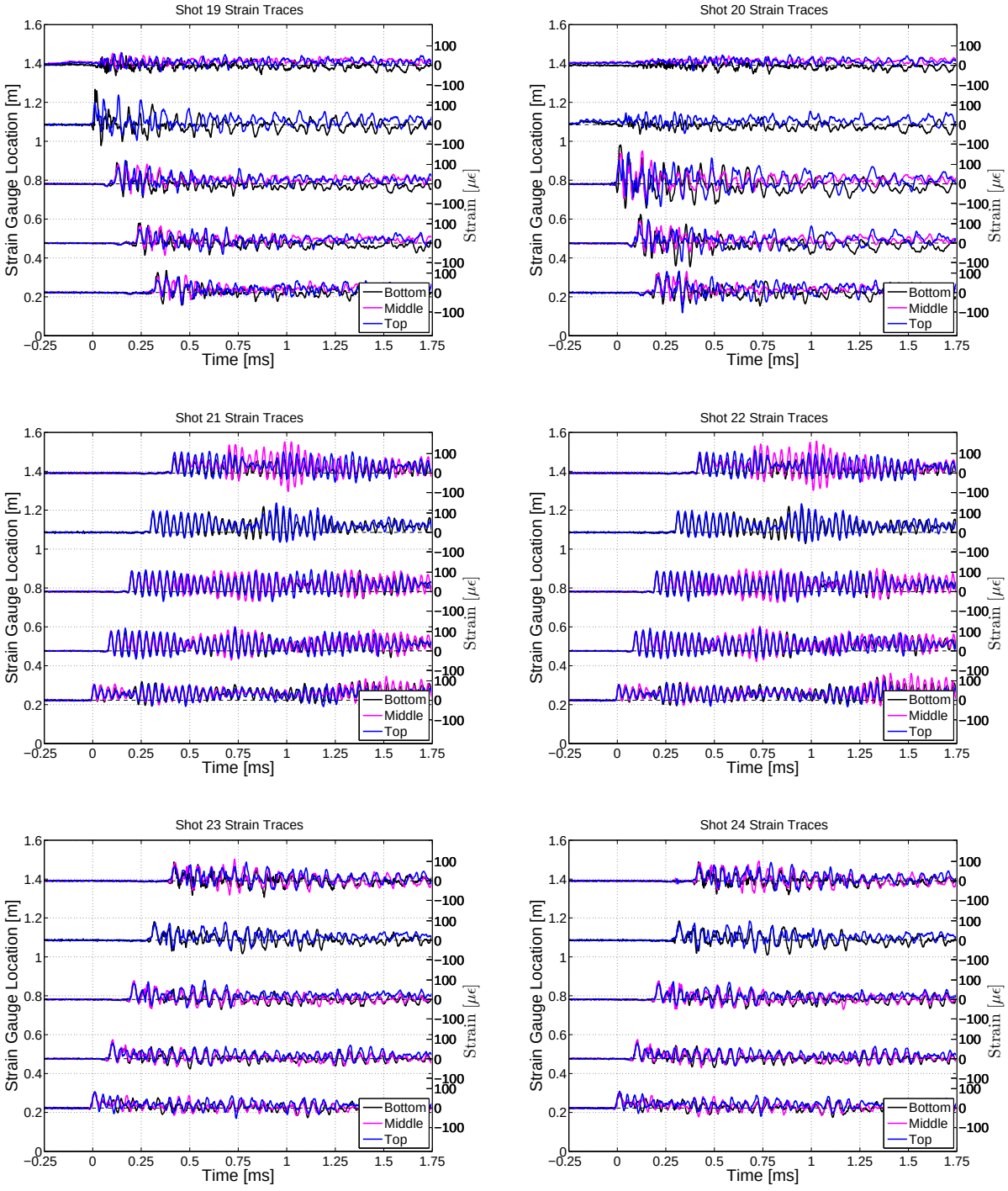

Figure 41: Strain Traces for shots 19-24

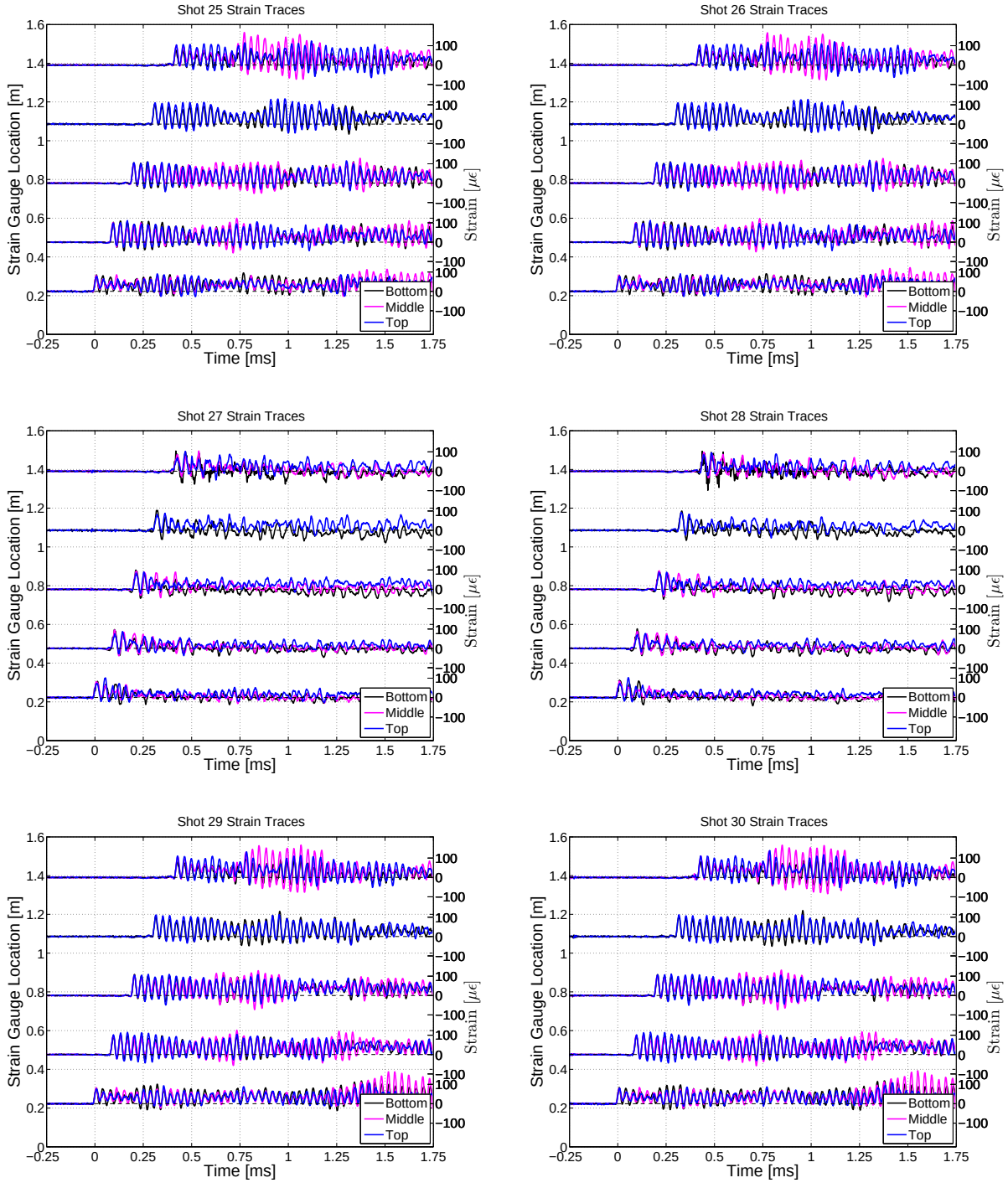

Figure 42: Strain Traces for shots 25-30

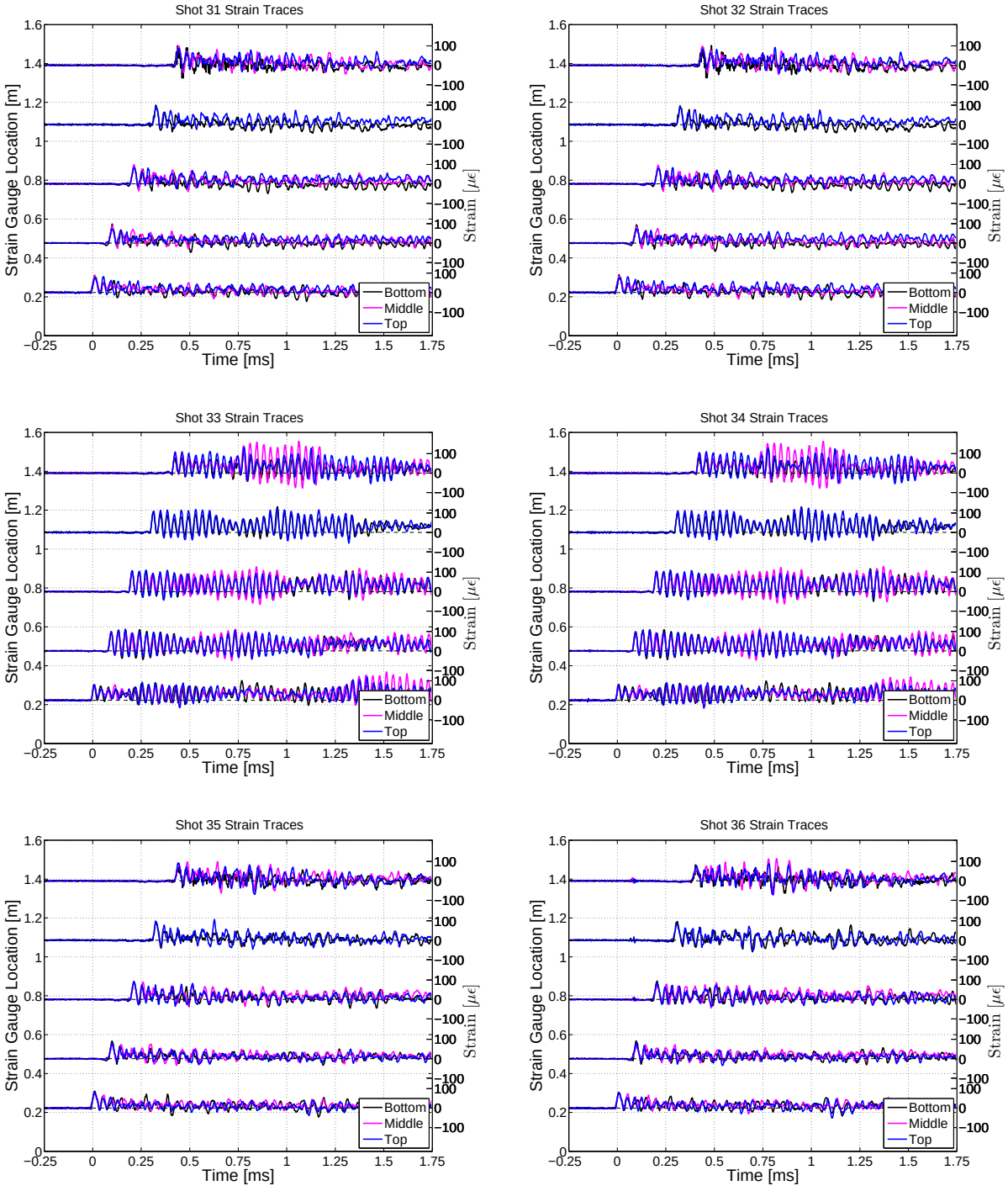

Figure 43: Strain Traces for shots 31-36

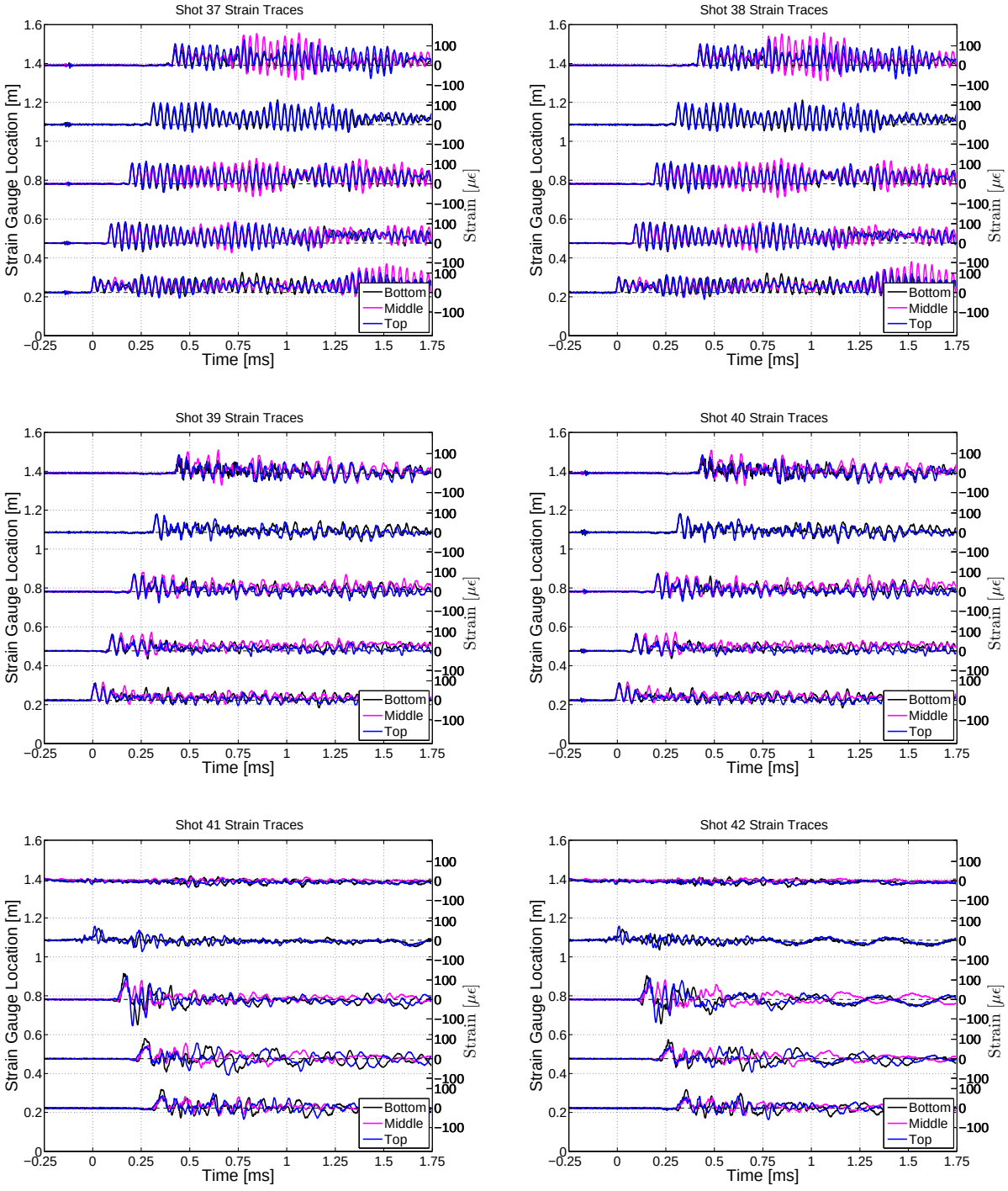

Figure 44: Strain Traces for shots 37-42

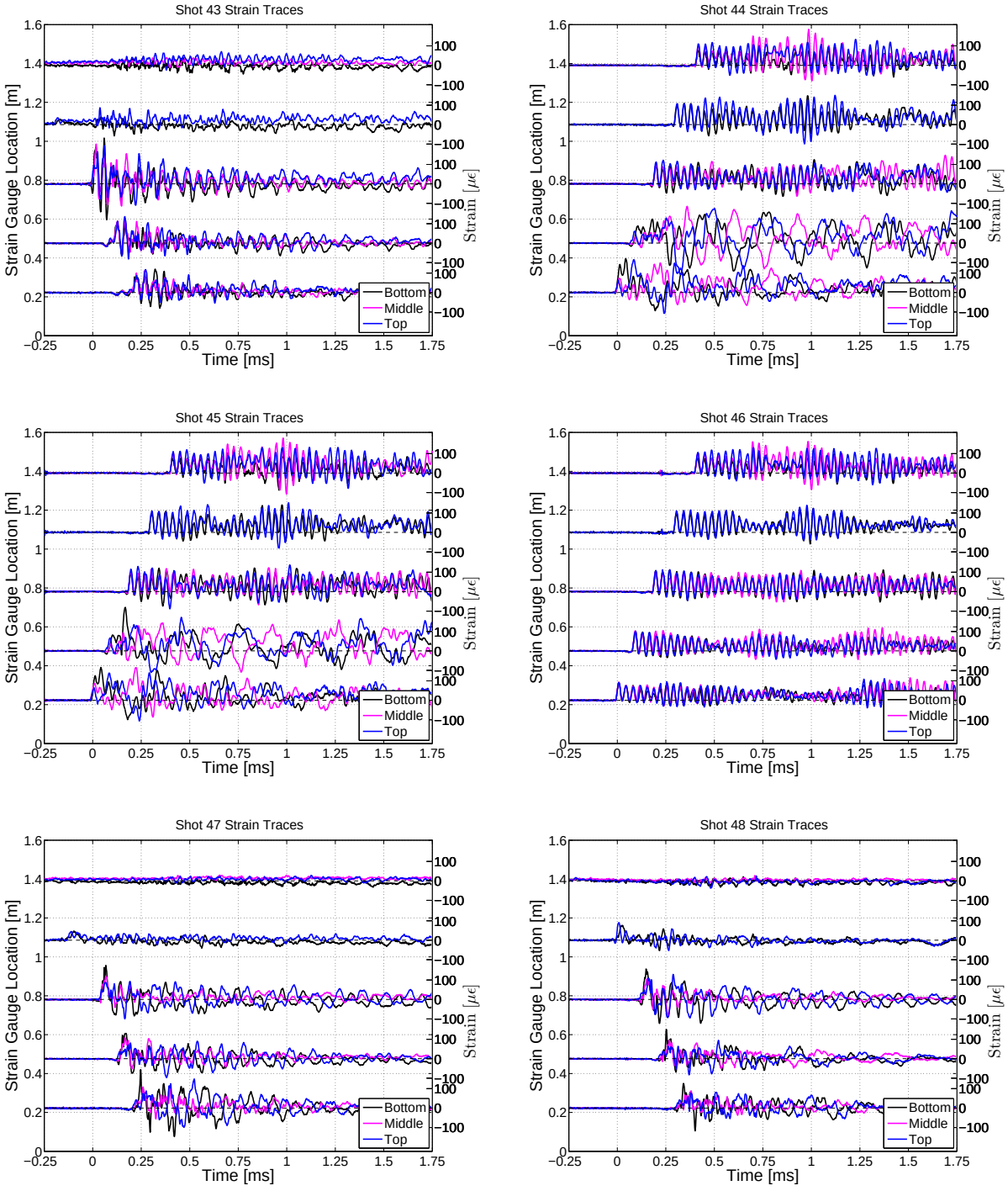

Figure 45: Strain Traces for shots 43-48

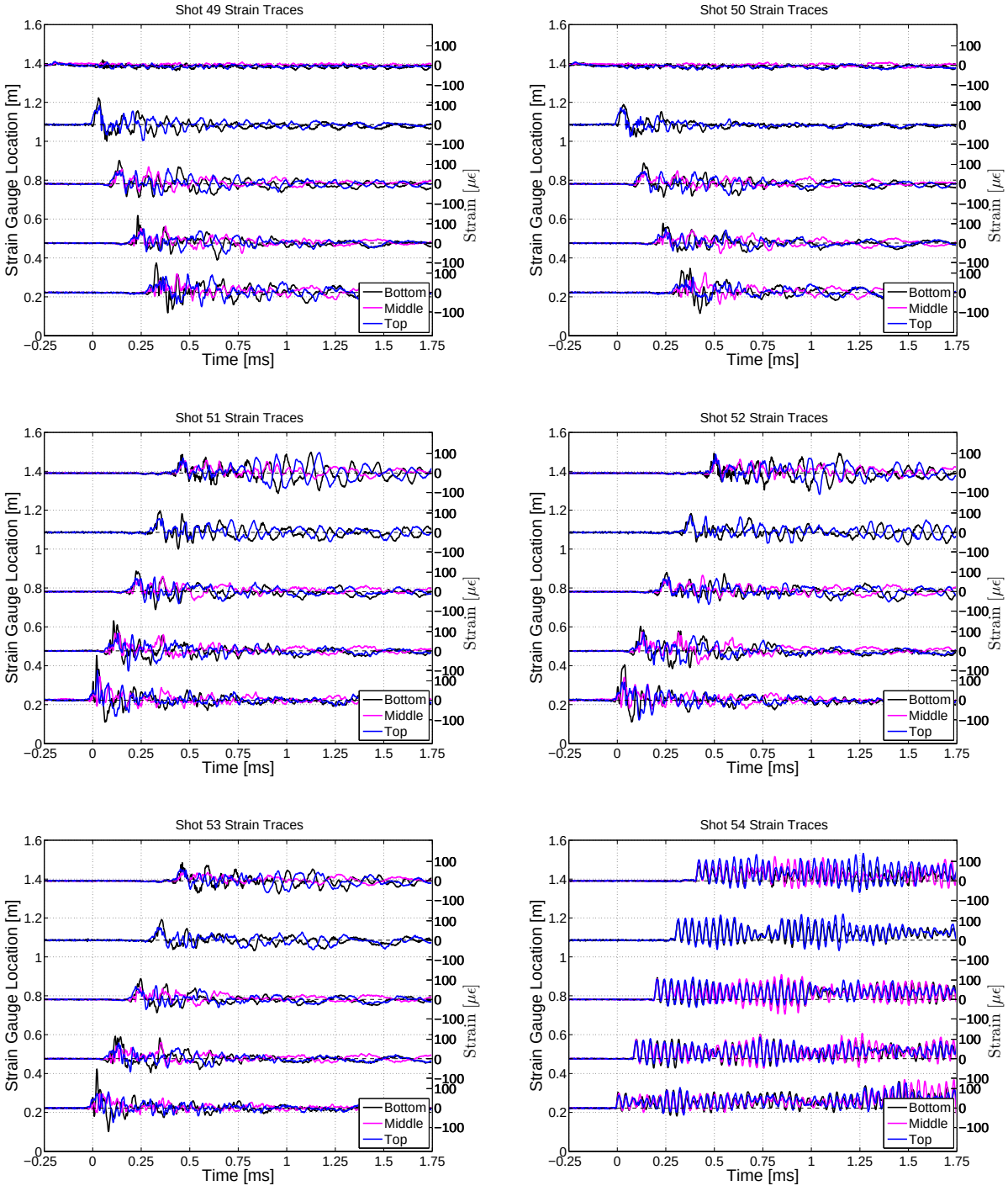

Figure 46: Strain Traces for shots 49-54

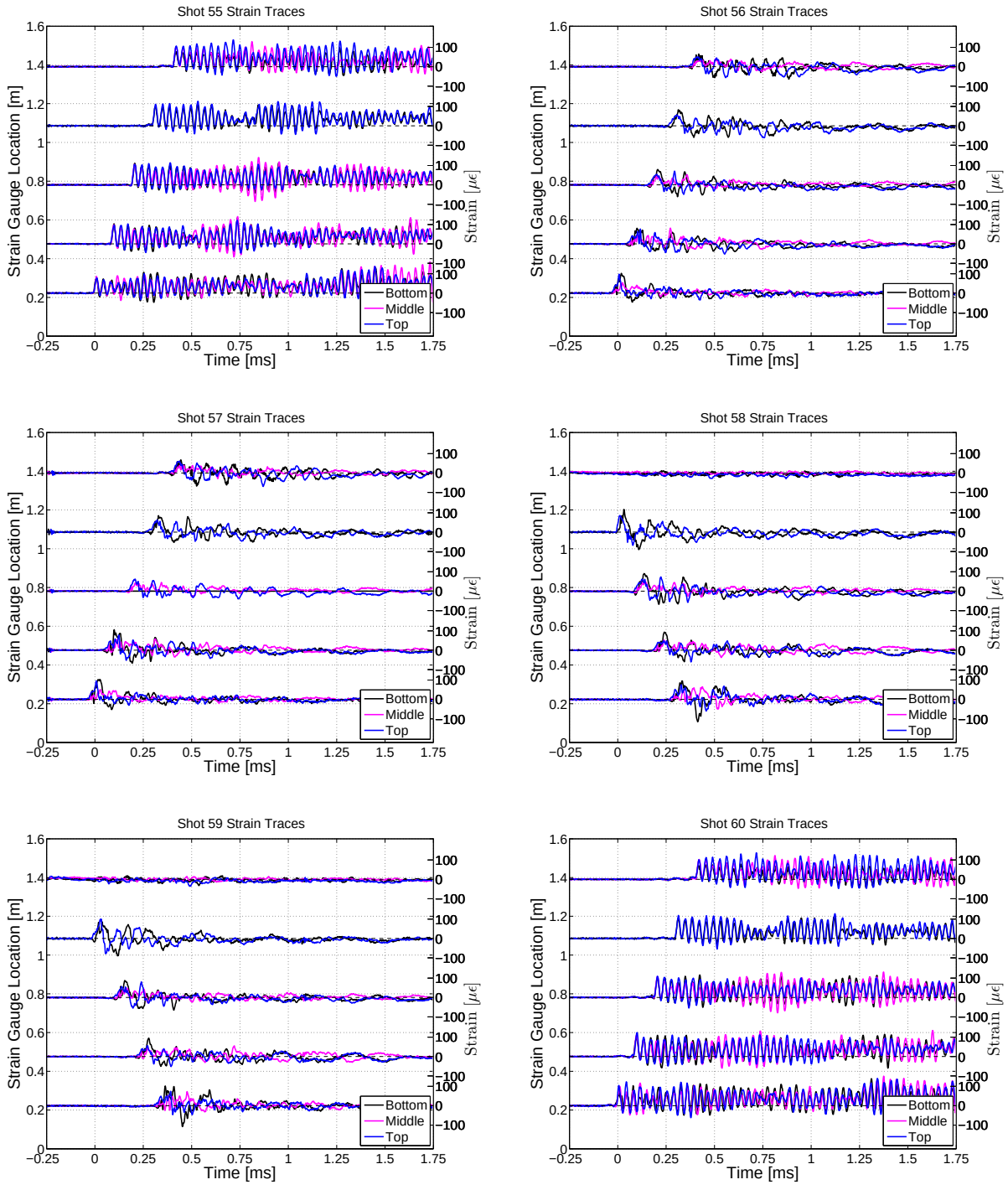

Figure 47: Strain Traces for shots 55-60

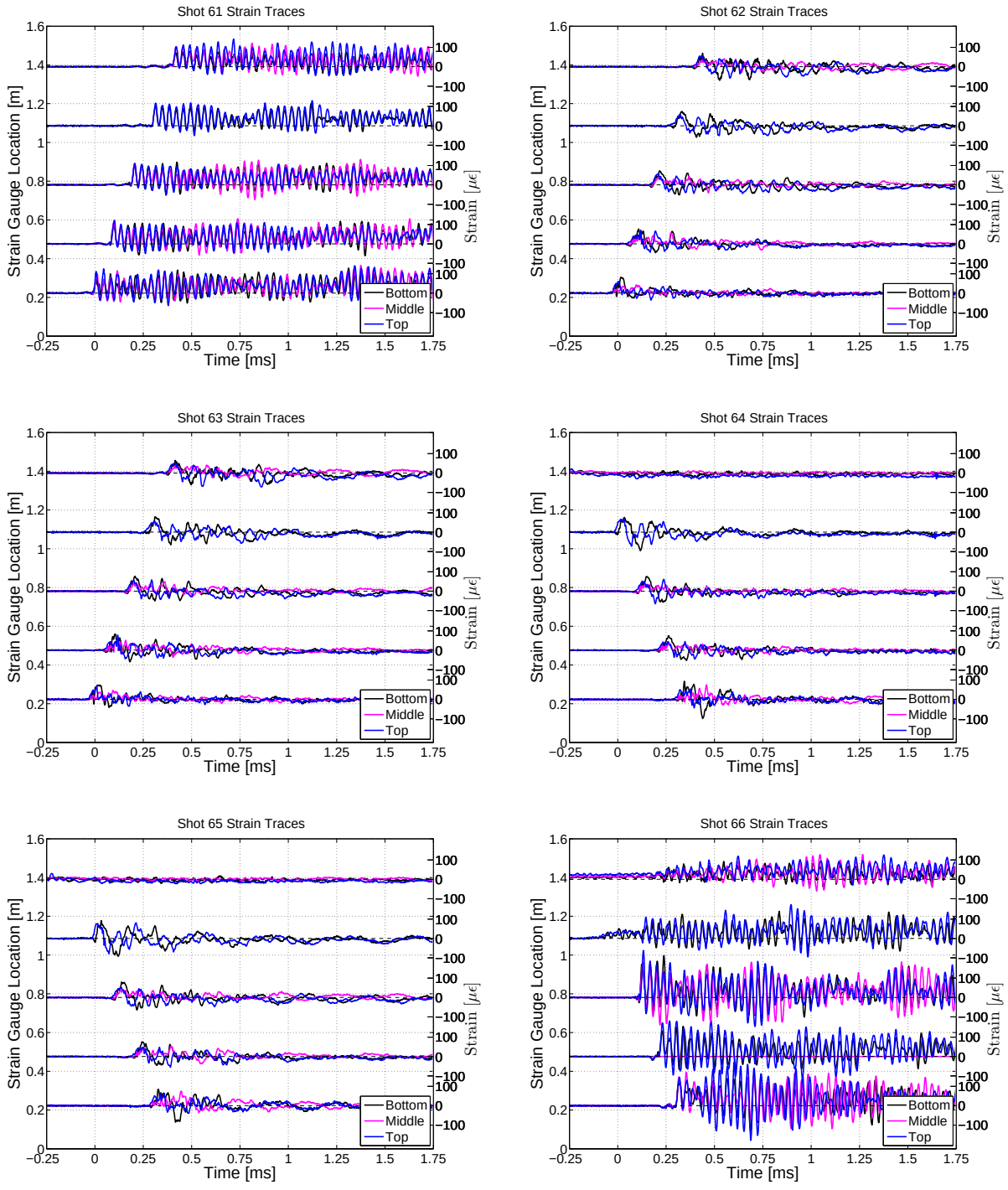

Figure 48: Strain Traces for shots 61-66

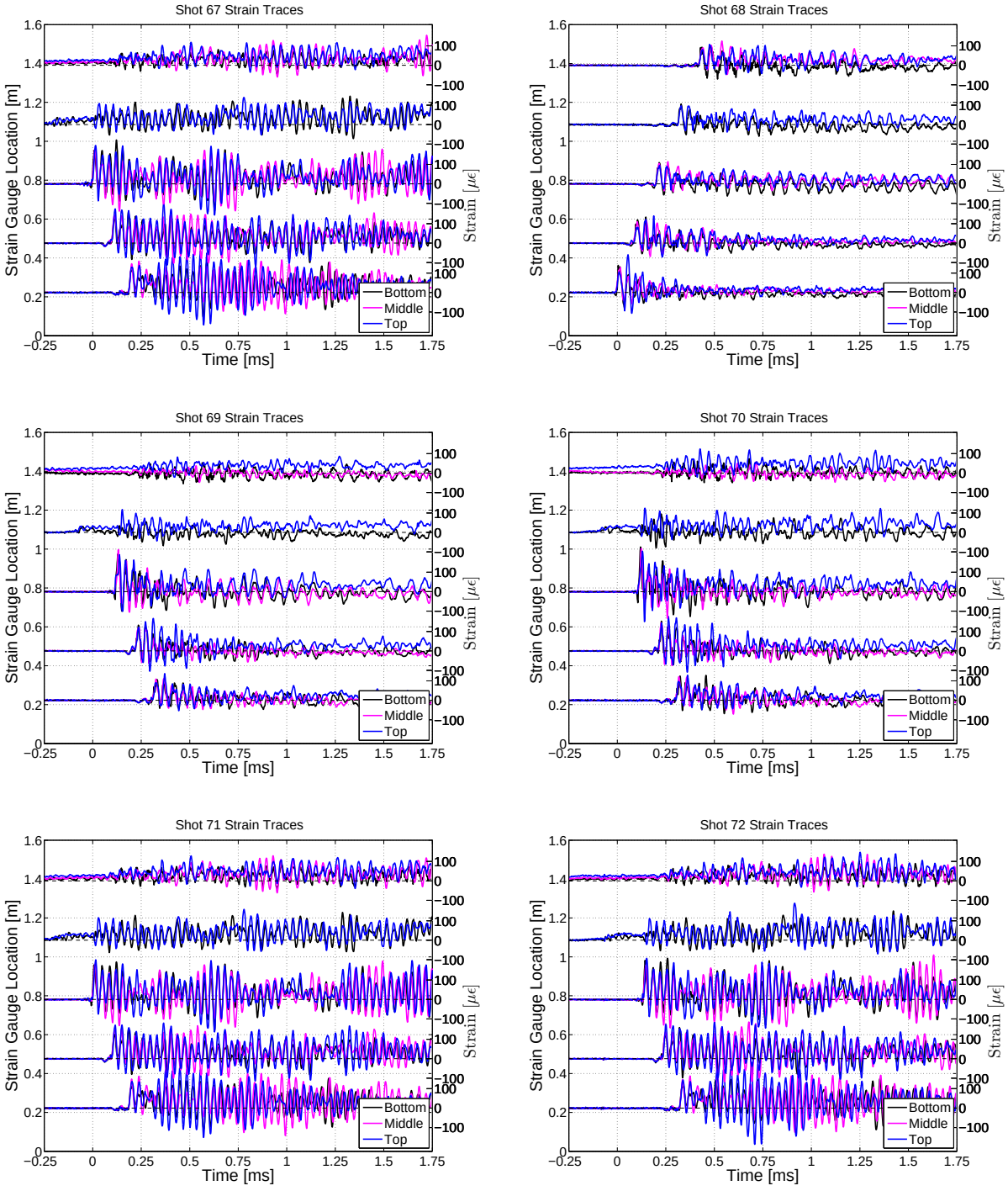

Figure 49: Strain Traces for shots 67-72

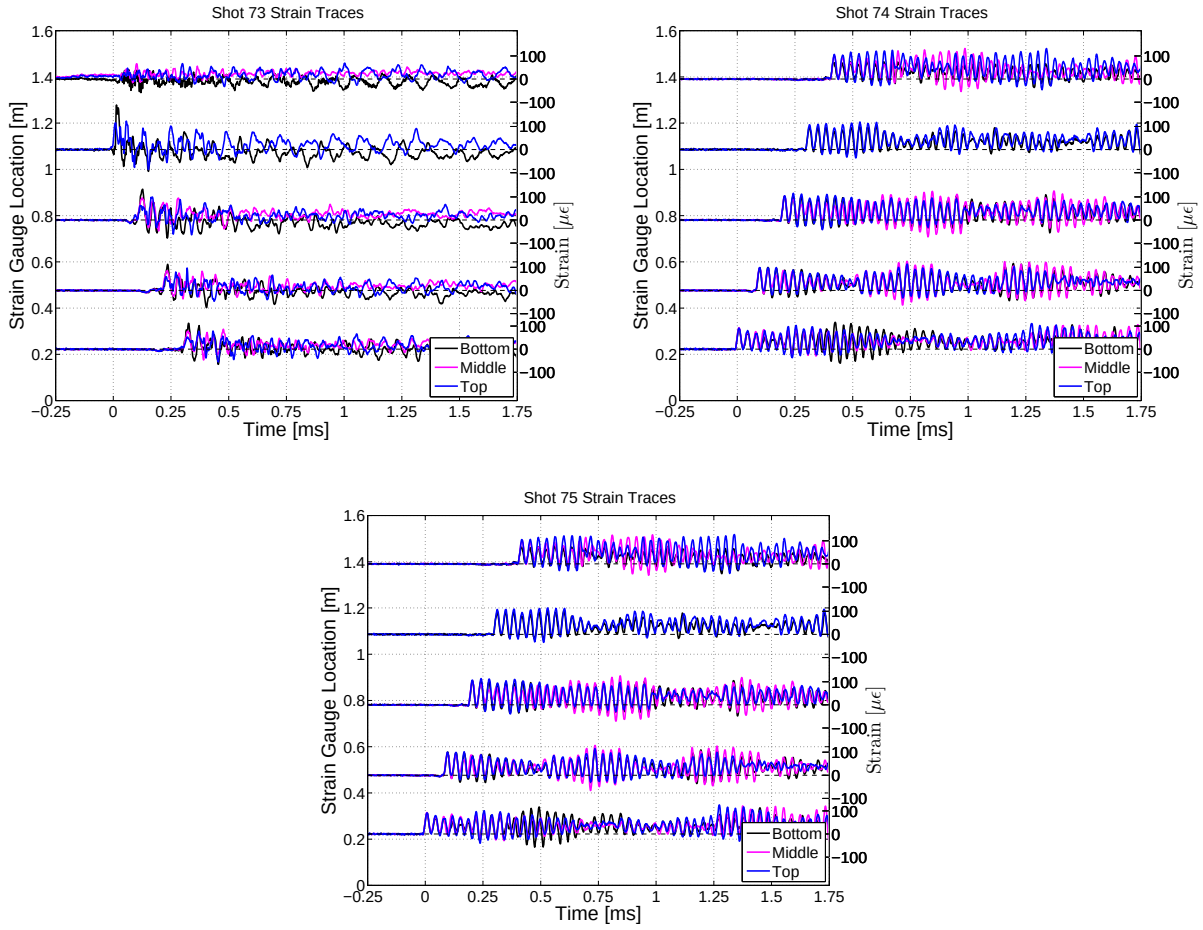

Figure 50: Strain Traces for shots 72-75